Nuclear Magnetic Resonance Sensors and Methods for Volume Status Monitoring

By

Chris J. Frangieh

B.E., Dartmouth College (2017)
B.A., Dartmouth College (2017)

Submitted to the
Department of Electrical Engineering and Computer Science
in Partial Fulfillment of the Requirements for the Degree of

Masters of Science in Electrical Engineering and Computer Science
at the
Massachusetts Institute of Technology

June 2019

Signature redacted

Signature of Author ....
Department of Electrical Engineering and Computer Science
May 7, 2019

Signature redacted

Certified by.....
Michael J. Cima
Professor, Department of Materials Science and Engineering
Thesis Supervisor

Signature redacted

Accepted by ....
Leslie A. Kolodziejski
Professor, Electrical Engineering and Computer Science
Chair, Department Committee on Graduate Students

Nuclear Magnetic Resonance Sensors and Methods for Volume Status Monitoring

By
Chris J. Frangieh

Submitted to the
Department of Electrical Engineering and Computer Science
on May 7, 2019
in Partial Fulfillment of the Requirements for the Degree of
Masters of Science in Electrical Engineering and Computer Science

Abstract

Portable, non-invasive sensors of tissue fluid distribution would aid in diagnosis of fluid volume disorders and inform therapeutic decisions across diverse patient populations. Existing techniques are inaccurate, invasive, or easily confounded by patient physiology. Single-sided magnetic resonance (MR) devices could provide a portable, low-cost platform for localized measurements of fluid distribution. This thesis demonstrates a single-sided MR sensor that can quantify fluid distribution of heterogeneous samples via depth-resolved, diffusion-weighted, multicomponent T2 relaxometry. Validation using synthetic tissue phantoms, ex vivo tissue samples, and an in vivo edema model is presented. Estimation of tissue fractions in heterogeneous samples with 2% error and tissue layer thickness with 0.1 mm error is demonstrated. The sensor can identify onset, progression, and recovery of muscle edema despite the presence of a confounding subcutaneous tissue layer. These methods can provide point-of-care diagnostics for fluid distribution disorders such as end-stage renal disease and dehydration.

Thesis Supervisor: Michael J. Cima
Title: Professor, Department of Materials Science and Engineering

Contents

List of Figures

1. Chapter 1: Introduction

This thesis explores the use of nuclear magnetic resonance (NMR) as a diagnostic tool for volume status disorders. A single-sided NMR device is characterized, and methods for improving diagnostic validity are explored. Improvements to existing protocols are validated using preclinical animal models. Finally, the broader clinical implications of this work are discussed along with suggestions for future improvements. Human data presented in this section was collected and analyzed by Lina Colucci.

1.1. *Nuclear Magnetic Resonance*

The NMR phenomenon begins with atoms possessing nuclear spin angular momentum in a main magnetic field, denoted B_0. The atoms align both parallel and antiparallel to the applied magnetic field, with a slight energy preference for the parallel state. The net magnetization is thus aligned with B_0. The atoms additionally exhibit precession at a well-defined frequency known as the Larmor frequency (ω). The Larmor frequency relates to the main magnetic field through the equation:

$$f = \frac{\gamma}{2\pi} B_0 \tag{1}$$

where γ is a physical quantity known as the gyromagnetic ratio. For ^{1}H, the atom of interest in this work and the atom most broadly studied in NMR, $\frac{\gamma}{2\pi} = 42.58 \frac{MHz}{Tesla}$ *(1)*.

A radiofrequency (RF) pulse tuned to the Larmor frequency of the spins is applied to a sample placed in the main magnetic field. Rotating the spins into the transverse plane causes subsequent relaxation towards the direction of the main magnetic field, known as the longitudinal axis. Time constants can be extracted from the sample by measuring relaxation along the longitudinal axis, namely T_1 relaxation, and by measuring relaxation in the transverse plane, namely T_2 relaxation *(1)*.

1.2. *Single-Sided NMR*

Portable, single-sided NMR devices are constructed by utilizing a unilateral magnet geometry. Portability allows single-sided devices to perform point-of-care diagnostics. The main magnetic field can be created by permanent magnets to decrease power requirements of the device. RF excitation and relaxation

measurements are performed using a single transceiver coil or separate transmit and receive coils. The RF excitation frequency is selected to excite spins in a homogenous region of the main magnetic field *(2)*.

1.3. *Preliminary Clinical Trial*

Our lab has previously demonstrated that MRI and portable magnetic resonance (MR) sensors can resolve individual fluid compartments (subcutaneous, intramuscular, etc.) within tissue. NMR relaxivity measurements as determined by either MRI or our MR sensors measure properties of water within the tissue *(3)*. The proton nuclear spin relaxation rate, due to magnetic field perturbation, depends on the mobility of the water molecule and, therefore, varies with tissue compartment. The amplitude of the signal from the relaxation process depends on the number of protons and, therefore, varies with the amount of water in each tissue compartment. The single voxel MR sensors that we design and construct measure the combined effects of all tissue compartments within the voxel. Our pilot study compared this approach to quantitative MRI. Quantitative MRI (qMRI) allows the relaxation measurement to be confined to a selected region of interest. qMRI is likely impractical for routine use in an HD clinical setting, but is an excellent benchmark to evaluate our sensors. Muscle was found to be a highly responsive fluid reservoir during periods of volume overload. Measurements isolated to the skeletal muscle are, therefore, a reliable estimate of patients' volume status. The qMRI measurement easily differentiated HD patients from healthy controls (HC) and reliably measured the change in volume before and after dialysis. The sensor design used in the pilot study had a voxel that incorporated portions of both muscle and subcutaneous tissue. Thus, the sensor measurement could reliably measure the signal change expected for each HD patient before and after dialysis but could not reliably differentiate among patients (HD and HC).

Intradialytic hypotension (IDH) occurs in up to 75% of hemodialysis (HD) patients which can cause nausea, vomiting, cramping, and chest pain. This negatively affects patient quality of life and reduces long-term compliance with HD prescription *(4)*. Increased morbidity of IDH includes bowel ischemia, stroke, fistula thrombosis, myocardial infarction which is associated with a 26% increase in mortality *(5,6)*. Myocardial stunning due to intradialytic hypovolemia induces changes such as fibrosis, remodeling, and hypertrophy, which are risk factors for future cardiac events *(7)*. Furthermore, repeated, acute cerebral ischemia is associated with cognitive decline and neurological disease (e.g. dementia) *(8)*. Long-term volume overload and poorly managed ultrafiltration rates are also common *(9,10)*. Clinicians and patients lack a simple and reliable tool to measure the extent of fluid

overload to assist with long-term fluid management.

Clinical assessments are subjective and, in many cases, unable to predict fluid overload *(11)*. For example, pedal edema, a commonly utilized clinical measure of volume overload, correlates poorly with many other more objective, resource-intensive measures of fluid overload *(12)*. Existing management efforts rely on weighing patients before each session. This technique does not resolve individual fluid compartments and is easily confounded by changes in nutrition, lean body mass, poor appetite, infection, and many other factors *(9,13)*. Other non-invasive approaches to assessing volume status, such as bioimpedance, ultrasound, and blood pressure, rely on systemic physiological changes rather than directly measuring fluid distribution. These methods therefore exhibit large interpatient and intrapatient variability *(13–15)*. These techniques cannot robustly characterize dynamics in the underlying physiology (i.e. interstitial fluid depletion as HD progresses).

The proposed technology will enable substantial improvements in fluid management for HD patients by providing a real-time assessment of volume status to clinicians. This information will enable improved control over volume status by allowing more accurate estimation of ultrafiltration and dry weight goals. Currently, dry weight – the lowest weight a patient can reach without hypotension – is estimated based on clinical assessment and a subjective trial-and-error process. Errors in dry weight estimation can leave patients in either a hypovolemic or hypervolemic state after a HD session. The proposed technology enables interstitial fluid in the intramuscular compartment to be directly measured. This provides a quantitative indicator of volume status and can be used to estimate dry weight. This technology will provide a real-time measure of fluid volume status to guide the fluid removal target. The measurement would provide actionable information to avoid intradialytic hypotension and its adverse effects such as bowel ischemia, stroke, fistula thrombosis, myocardial infarction and stunning. Adaptive fluid removal protocols are critical to reduce incidence of adverse events such as hypotension. Chronic hypervolemia is associated with many adverse effects and existing measurement approaches rely upon easily confounded and subjective assessments *(12)*. The technology would improve long-term HD treatment by providing clinicians with a quantitative metric of patients' progress over multiple HD sessions. This technology could ultimately serve as a patient-based quality assessment tool.

We have successfully designed and built an MR sensor consisting of a Unilateral Linear Halbach magnet array (0.2 Tesla) contained in a custom housing, a custom RF transceiver coil, and a spectrometer for pulse generation. The device can

perform measurements with single shot SNR of 15 at a depth of 5 mm. The design methodology for this device is detailed in recent publications *(16–18)*. Here we explore a next generation sensor design to enable significantly deeper measurements to be made. Our preliminary sensor has shown strong agreement with standard clinical MRI in measuring T2 relaxation times, the MR parameter of interest, of synthetic models of tissue.

We have successfully measured changes in fluid distribution in ESRD patients (N = 7) and in healthy controls (HC) (N = 7) with both clinical MRI and our custom sensor. Quantitative T2 MRI scans were processed by performing a pixelwise biexponential fit which produces two unique T2 relaxation times and an associated amplitude for each relaxation time. Separating muscle pixels from subcutaneous fat pixels and performing a biexponential fit on each pixel indicates a clear distinction in T2 relaxation times between muscle tissue and subcutaneous fat tissue **(Figure 1a)**.

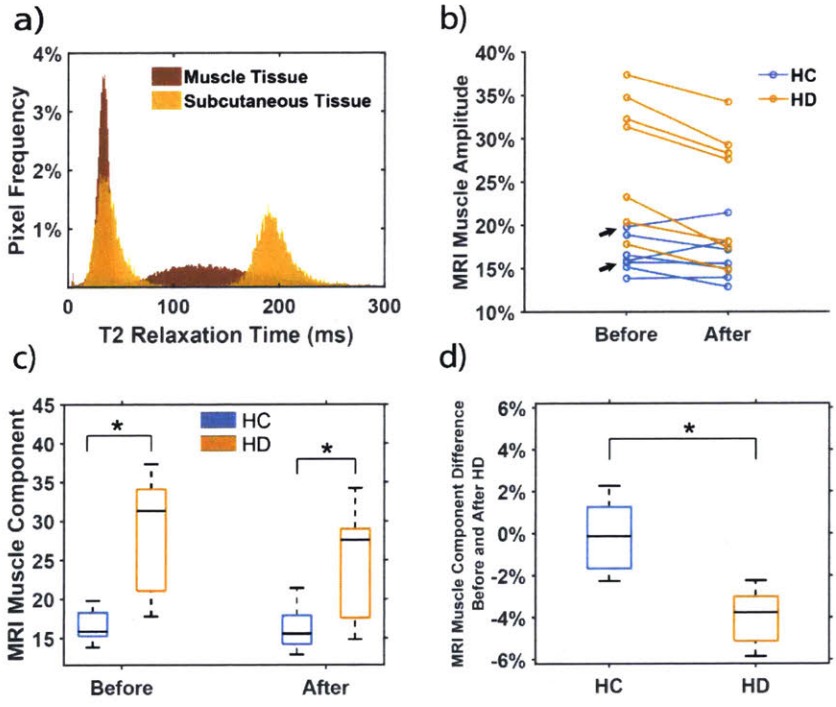

Figure 1. Summary of clinical MRI data. a) A pixel-wise fit of a lower leg MRI scan demonstrates clearly distinguishable muscle and subcutaneous compartments. **b)** The change in MRI muscle signal amplitude for healthy control (HC) patients (N = 7) and hemodialysis (HD) patients (N = 7). The muscle amplitude in HC patients decreased after bedrest for all but two patients who were dehydrated at the start of the experiment (black arrows). Bedrest with fluid restriction causes fluid loss indicating MRI is able to detect subtle volume changes using the muscle compartment. **c)** HC and HD muscle component in the MRI before and after a rest period or HD. MRI data can distinguish HD patients from HC patients prior to and following HD based on the amplitude of the muscle signal. **d)** The percent change in muscle component signal for HC and HD. MRI data can distinguish between the two populations. The central mark in each box indicates the median, and the bottom and top edges of

the box indicate the 25th and 75th percentiles, respectively. The whiskers extend to the maximum and minimum values. Asterisks indicate statistical significance ($p < 0.05$).

A pixelwise biexponential fit was performed on the muscle compartment of lower leg MRI images. The muscle amplitude in HC patients decreased after bedrest for all but two patients who were dehydrated (per blood serum osmolality and serum sodium) at the start of the experiment **(Figure 1b)**. Bedrest with fluid restriction causes fluid loss indicating MRI is able to detect subtle volume changes using the muscle compartment. There is a statistically significant population difference between HCs before and after four hours of bedrest and HD patients before and after HD, respectively **(Figure 1c)**. There is also a statistically significant difference in the signal change between the two populations **(Figure 1d)**. Using body weight change as an estimate of fluid loss, HC lost an average of 0.6 L of fluid during bedrest while HD patients lost an average of 2.2 L of fluid throughout the course of HD. Signal change due to fluid loss is, therefore, localized to the muscle compartment. This demonstrates that HD more strongly affects the fluid distribution in muscle than in subcutaneous tissue. Secondly, the data **Figure 1c** support the conclusion that states of hypervolemia and euvolemia (HD and HC, respectively) are characterized by specific fractions of interstitial fluid in the muscle compartment. This result was independent of the muscle chosen.

A triexponential fit was used to process MR sensor results. The histogram of MRI pixel by pixel fits **(Figure 1a)** indicates that the fastest T2 relaxation time is shared by muscle and fat components, the middle T2 relaxation time corresponds primarily to muscle tissue, and the longest relaxation time to subcutaneous tissue. Our current sensor has a sensitive region 2 mm deep located approximately 3 mm distal from the surface of the magnet. MRI images of HD patients indicate the depth of combined skin and subcutaneous fat tissue can vary from 3.5 to 6 mm, indicating the distance from the sensor surface to the muscle tissue varies. The longest T2 relaxation time is stronger when measuring larger volumes of subcutaneous tissue in measurements from the portable MR sensor **(Figure 2)**. Agreement between the T2 relaxation time distributions between MRI and our sensor indicates the ability of our sensor to correlate with clinically significant outcomes.

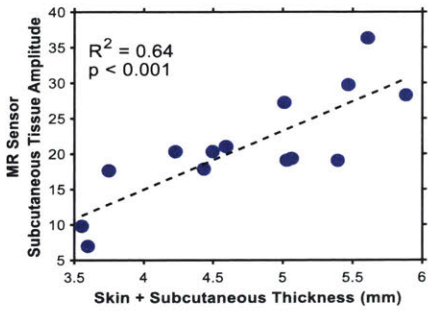

Figure 2. Skin and subcutaneous thickness versus MR sensor subcutaneous tissue signal. A thicker subcutaneous compartment accounts for a larger proportion of the MR sensor signal confounding measurements of muscle.

Single-sided measurements of HD patients are, therefore, expected to most strongly predict fluid loss when the combined skin and subcutaneous fat depth is sufficiently small to allow for measurement of the muscle compartment. As combined skin and subcutaneous fat depth increases, the signal from subcutaneous tissue accounts for a larger proportion of the total signal **(Figure 2)**.

Our device was able to establish a statistically significant difference between the change in the muscle signal amplitude between HC and HD populations **(Figure 3b)**. The same measurement, however, was unable to distinguish between healthy patients and HD patients **(Figure 3a)**. Our initial device was unable to reproduce results generated by MRI because it was not designed for measurement of the muscle compartment.

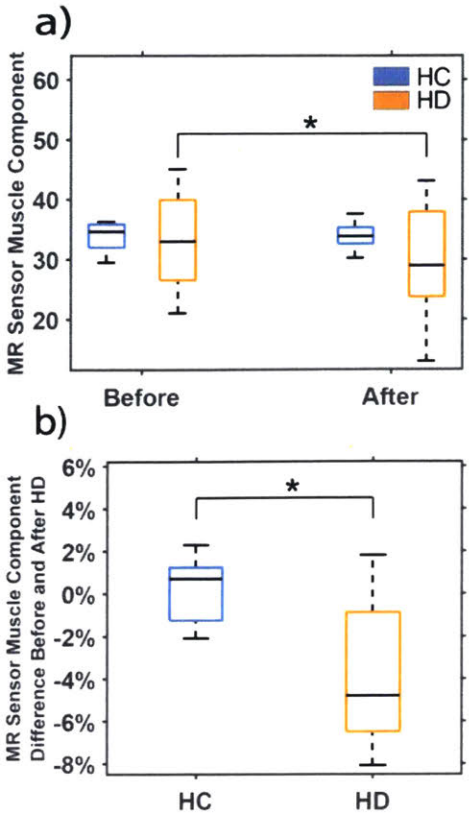

Figure 3. Summary of clinical MR sensor data. a) The change in MR sensor muscle signal amplitude for healthy control (HC) patients (N = 7) and hemodialysis (HD) patients (N = 7). MR data cannot distinguish the HD patient population from the HC patient population, but can distinguish the AM HD population from the PM HD population. **b)** The percent change in muscle component for HC and HD. MR data can distinguish the two populations using percent change. The central mark in each box indicates the median, and the bottom and top edges of the box indicate the 25th and 75th percentiles, respectively. The whiskers extend to the maximum and minimum values. Asterisk indicates statistical significance ($p < 0.05$).

1.4. *Thesis Overview*

This thesis prevents characterization and *in vivo* validation of our single-sided NMR device. Chapter 2 characterizes the sensitivity profile of the device and demonstrates multicomponent T2 relaxometry, depth profiling, diffusion weighting, and muscle fraction estimation. Chapter 3 presents validation of the techniques described in Chapter 2 via a rodent model of acute muscle edema. Chapter 4 concludes the thesis with a discussion of the clinical impact of this work and suggestions for future work.

2 Chapter 2: Device Characterization

Chapter 2 present characterization of the ssNMR sensor. Methods for improving measurement of muscle tissue are multicomponent T2 relaxometry, RF excitation frequency tuning, and diffusion weighting. This chapter presents supporting data for each of these techniques prior to *in vivo* validation. Data presented in this chapter was collected, analyzed, and described in collaboration with Ashvin Bashyam.

2.1. *Device Sensitivity Profile*

A portable magnetic resonance sensor capable of measuring the fluid distribution within tissue via multicomponent T2 relaxometry was previously designed and built **(Figure 4a)**. This sensor was designed and constructed with a permanent magnet array to generate a static magnetic field (B_0) based on the Unilateral Linear Halbach array **(Figure 4b-c)** *(17)*. This sweet spot magnet design enables high sensitivity measurements over a large uniform region compared to more commonly used high gradient designs *(19)*. Permanent, rare earth magnets provide a means to generate a static magnetic field while also allowing for cost effectiveness, low maintenance, minimal power requirements, and portability compared to the more traditional superconducting magnets found in MRI. Furthermore, the magnetic field is parallel to the surface of the sensor allowing for the use of a standard radiofrequency (RF) transceiver coil in order to maximize sensitivity. The magnet produces a uniform region with a magnetic field strength of 0.28 Tesla located approximately 2 to 7 mm from the surface of the sensor as modeled by field simulations and experimentally confirmed with an acquired field profile **(Figure 4c)**. The sensitivity of the system was characterized by measuring the relative signal amplitude from a sample scanned through the sensitive region **(Figure 5)**. The sensor is sensitive towards a region located directly above the RF coil spanning a volume of 12 × 5 × 2 mm **(Figure 4d-e)**. This allows localization of the measurement towards skeletal muscle tissue while reducing any confounding signal from subcutaneous tissue *(20)*.

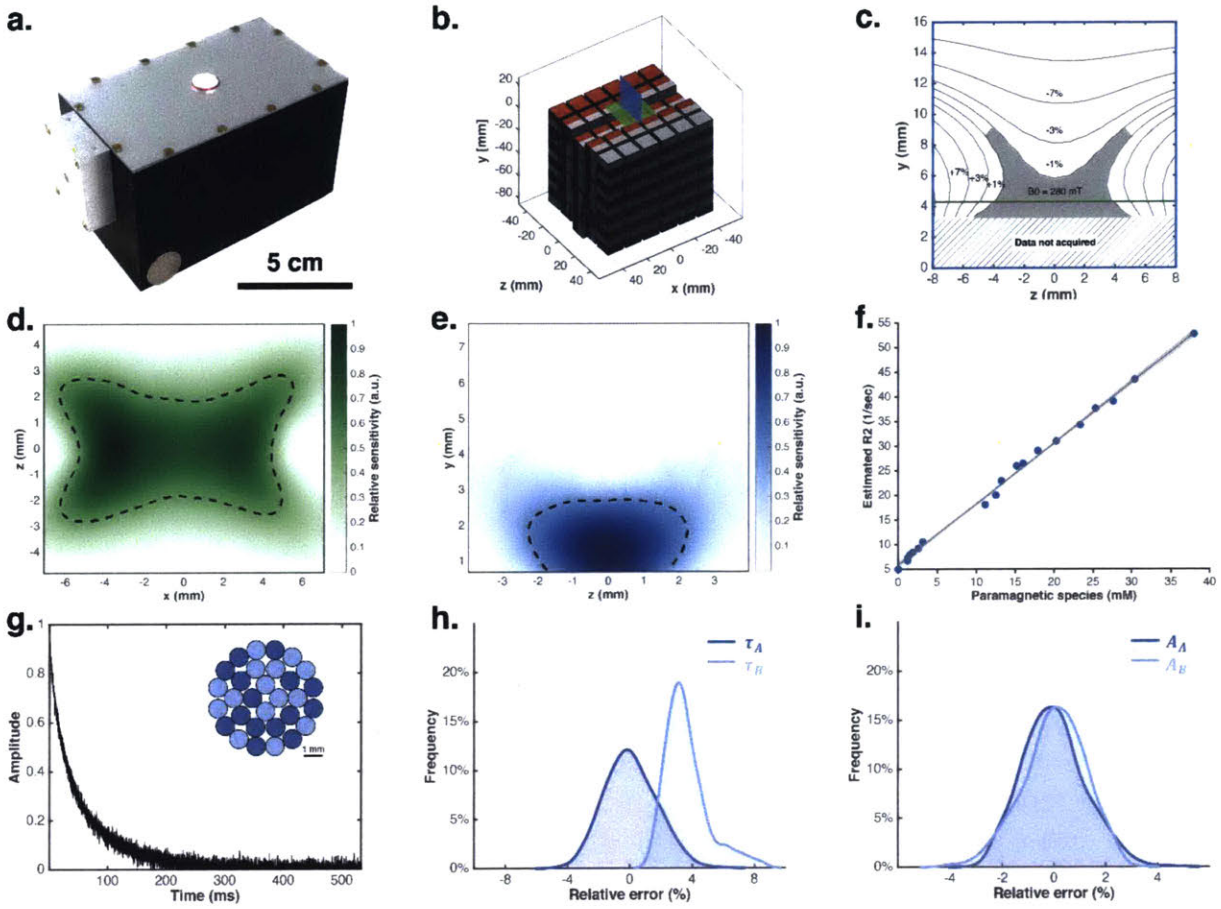

Figure 4. Portable magnetic resonance sensor identifies and quantifies fluid compartments via multicomponent T2 relaxometry. a) Fully assembled sensor with RF matching circuit and solenoidal transceiver coil. **b)** Illustration of Unilateral Linear Halbach permanent magnet array design for sensor. Red and grey shading indicates positive and negative poles, respectively, of each magnet. **c)** Measured static magnetic field profile directly above center of magnet. Shaded region indicates predicted sensitive region. **d-e)** Relative sensitivity of sensor across the **d)** xz-plane and the **e)** yz-plane indicates a 12 × 5 × 2 mm sensitive region. Shaded green and blue planes in **(b)** indicate relative orientation of measurement planes. Dashed lines indicate 50% relative sensitivity from the peak of the measurement region. **f)** Linearity of R2 relaxometry measurements with portable MR sensor versus paramagnetic species concentration. Shaded region indicates the standard deviation of the error of the linear fit ($n = 19$, $R^2 = 0.997$, $p < 1\times10^{-22}$, statistics by t test). **g)** MR signal acquired with CPMG acquisition from a synthetic tissue phantom comprising equal parts fast (24 ms, dark blue) and slow (84 ms, light blue) fluid compartments. Inset illustrates cross section of phantom. **h-i)** Analysis of each component with a biexponential model demonstrates accurate identification and quantification of the decay rate (τ_A, τ_B) and relative amplitude (A_A, A_B) of each component. Repeated trials yield histograms of estimation error.

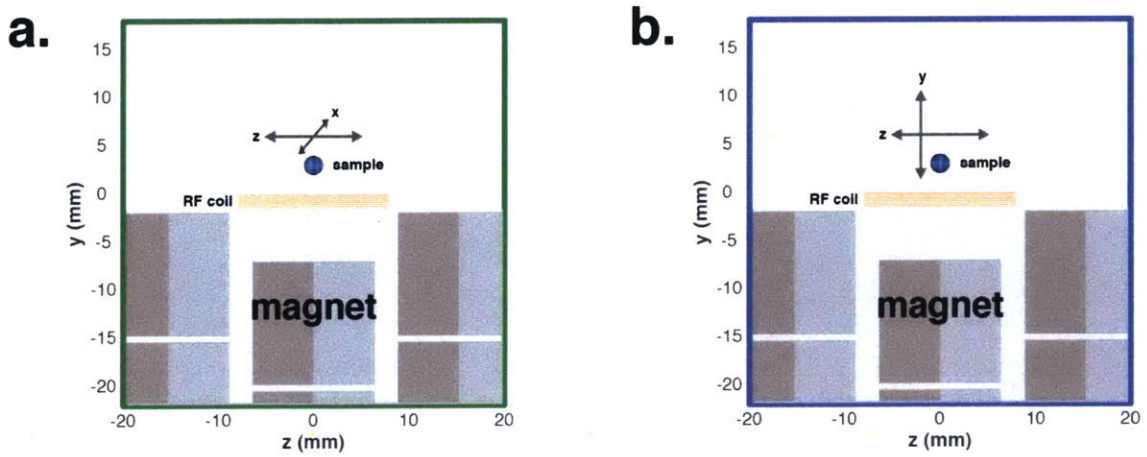

Figure 5. Illustration of sensitivity profile characterization of portable MR sensor. Experimental schematic for MR sensor sensitivity profiles along **a)** xz-plane and **b)** yz-plane. A 3 mm spherical bulb of CuSO4 aqueous solution was scanned across the measurement plane. The amplitude of the peak corresponding to the solution indicated the signal strength originating from the contents of the bulb.

The portable MR sensor reliably demonstrates the linear relationship between transverse (T2) relaxation rate and concentration of paramagnetic species ($CuSO_4$) in aqueous solution, a representative synthetic tissue phantom, using a CPMG (Carr-Purcell-Meiboom-Gill) pulse sequence for acquisition ($n = 19$, $R^2 = 0.997$, $p < 1\times10^{-22}$, statistics by t test) **(Figure 4f)**. There is a linear relationship between sample concentration and estimated relaxation rate across a wide range of concentrations per Bland-Altman analysis ($n = 19$, mean of differences = 0.0008, 95% confidence interval = -0.008 to 0.009, $p = 0.21$, statistics by significance of Spearman rank correlation of means and differences). These results are validated against a gold-standard benchtop NMR spectrometer (minispec mq7.5, Bruker, USA) further demonstrating validity of our portable sensor **(Figure 6)**. The estimated relaxation rates from the two MR systems are linearly related ($n = 19$, $R^2 = 0.996$, $p = 1\times10^{-12}$, statistics by t test). There is no bias in estimation of relaxation rates across a wide range of concentrations per Bland-Altman analysis indicating strong agreement between the two measurements ($n = 19$, mean of differences = -0.004, 95% confidence interval = -0.012 to 0.004, $p = 0.70$, statistics by significance of Spearman rank correlation of means and differences).

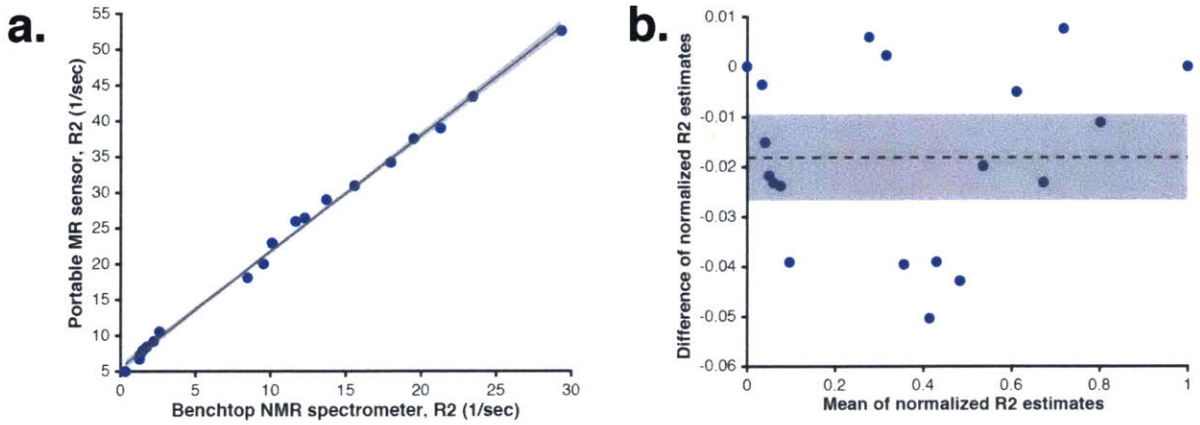

Figure 6. Validation of T2 relaxometry measurements from portable MR sensor with benchtop NMR spectrometer. a) The estimated relaxation rates from the two MR systems are linearly related (n = 19, R^2 = 0.996, p = 1×10^{-12}, statistics by t test). Shaded region indicates the standard deviation of the error of the linear fit. Residuals of a linear fit between the relaxation rate estimates between the two MR systems are approximately normally distributed (n = 19, p = 0.768, Lilliefors test for normality). **b)** There is no bias in estimation of relaxation rates across a wide range of concentrations per Bland-Altman analysis indicating strong agreement between the two measurements (n = 19, mean of differences = -0.004, 95% confidence interval = -0.012 to 0.004, p = 0.70, statistics by significance of Spearman rank correlation of means and differences).

A heterogeneous synthetic tissue phantom consisting of two distinct compartments with unique T2 relaxation rates was measured using the portable MR sensor **(Figure 4g)**. Relaxation time constants and relative amplitudes of each fluid compartment can be accurately and reproducibly extracted from signals acquired by the MR sensor via T2 relaxometry **(Figure 4h-i)**. This exemplifies the ability to accurately quantify fluid distribution across a heterogeneous sample via a single-sided portable MR sensor.

2.2. *Multicomponent T2 Relaxometry*

CPMG T2 decay curves were modeled as multiexponential signals in order to extract relaxation times (τ_i) and relative amplitudes (A_i). Echo integrals were computed as the sum of the points sampled for each echo during CPMG when more than one point was collected for each echo. A general multicomponent exponential decay signal was represented as:

$$\hat{y}(t, \boldsymbol{A}, \boldsymbol{\tau}) = \sum_{i=1}^{N} \boldsymbol{A}_i * exp(-t/\boldsymbol{\tau}_i) \quad \textbf{(2)}$$

where $\hat{y}(t)$ is the estimated signal, N is the number of components, **A** is a vector of amplitudes, and $\boldsymbol{\tau}$ is a vector of corresponding relaxation times. Two models were

used to represent the multicomponent nature of these signals in this study. The first optimizes over both the relaxation times and relative amplitudes. The optimal set of parameters is found by minimizing the L2-norm of the residuals between the estimated and the measured signal:

$$\boldsymbol{A}^{opt}, \boldsymbol{\tau}^{opt} = \underset{\boldsymbol{A},\boldsymbol{\tau}}{\operatorname{argmin}} \|y(t) - \hat{y}(t)\|_2 \quad \textbf{(3)}$$

where $y(t)$ is the measured signal and $\|.\|_2$ represents the L2-norm. This model allows discovery of the relaxation times and amplitudes of a multiexponential signal. The second model optimizes only over the amplitudes as the relaxation times are specified as parameters:

$$\boldsymbol{A}^{opt} = \underset{\boldsymbol{A}}{\operatorname{argmin}} \|y(t) - \hat{y}(t, \boldsymbol{\tau})\|_2 \quad \textbf{(4)}$$

This more constrained model allows the amplitudes to be estimated more accurately and differences between signals to be described solely as amplitude changes. Signal to noise ratio (SNR) was defined as the maximum magnitude value divided by the standard deviation of the noise. The noise distribution was estimated from the residuals of the fit.

The presence of signals from multiple tissues, especially when each produces a distinct multicomponent T2 decay signal, can confound the analysis of a single tissue. Identifying the contribution from each tissue to the measurement allows isolation of each of their signals and further analysis of their relaxation properties.

We demonstrate the identification of tissue fractions from an MR signal acquired with the portable MR sensor. Muscle and fat tissue were extracted from a rat and measured with the CPMG pulse sequence on the sensor to establish reference signals **(Figure 7a)**.

Tissue was extracted from a Sprague Dawley rat immediately after euthanasia via carbon dioxide inhalation. Muscle and fat tissue was excised from the lower hind limb. Tissue was gently blotted dry with a paper towel to remove excess moisture. Tissue samples were placed into sealed containers to avoid evaporation during MR measurements. In order to prepare the hybrid sample, fresh tissue samples were cut into small (~1 mm) pieces, weighed, combined into a heterogeneous mixture, and placed into a sealed container.

Portable MR sensor measurements were performed with the CPMG pulse sequence with 8192 echoes, an RF excitation frequency of 11.60 MHz, an echo time of 65 µs, a

repetition time of 1517 ms, a pulse duration of 12 µs, an acquisition bandwidth of 1 MHz (dwell time of 1 µs), and 16 acquired points per echo with a Kea2 spectrometer (Magritek, Wellington, New Zealand).

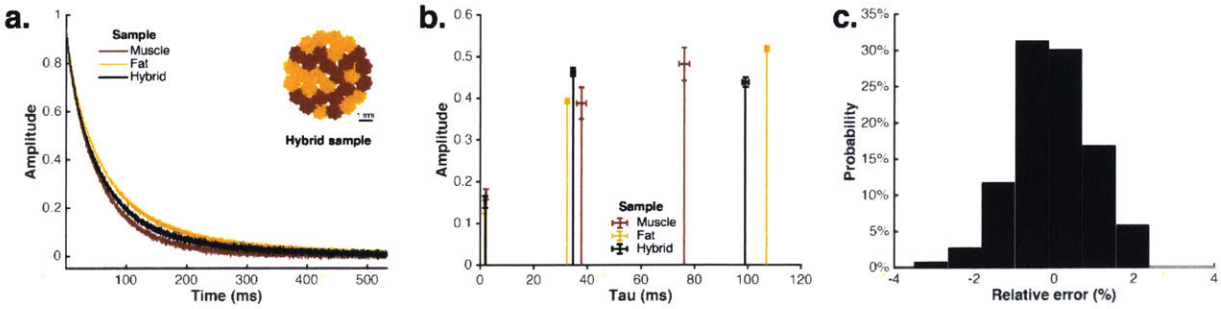

Figure 7. Multicomponent T2 relaxometry allows estimation of tissue fraction from a heterogeneous sample. a) Time domain CPMG decay curves and **b)** triexponential relaxation peaks of signal acquired from ex vivo muscle, fat, and hybrid sample. Inset in **(a)** illustrates a cross-section of the hybrid sample. Error bars in **(b)** indicate 95% confidence intervals on parameter estimates. **c)** A histogram indicating the distribution of estimation errors of the constituent tissue fractions within the hybrid sample upon repeated trials.

The signals from fat and muscle decay at different rates. Triexponential fits **(3)** of these decay curves show that the relaxation peaks are distinct between muscle and fat **(Figure 7b)**. A hybrid sample comprising a mixture of muscle and fat tissue has a decay rate between that of its constituent signals **(Figure 7a)**.

A multiexponential fit of all of the relaxation times from both muscle and fat fails to appropriately assign amplitudes to each of the six constituent relaxation peaks. Parameter extraction from multiexponential decays is an ill-posed problem, especially when some decay rates are similar. This problem is further exacerbated by the presence of noise. Furthermore, a triexponential fit is sufficient to fully model the multiexponential nature of the hybrid signal, as its residuals are very similar to those of a six exponential fit **(Figure 8)**. The relaxation peaks of the hybrid sample are each between those of muscle and fat when fit as a triexponential signal **(Figure 7b)**. Attempting to use the amplitudes produced by the triexponential fit as an estimate of the relative fraction of muscle and fat within the hybrid signal is not possible as each relaxation peak has an unknown contribution from both constituent signals.

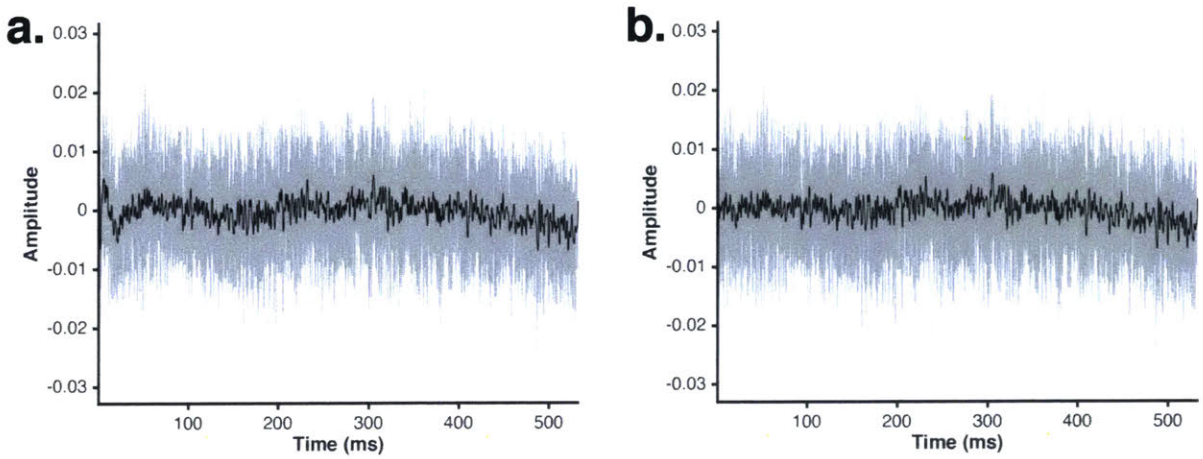

Figure 8. Residuals of ex vivo tissue hybrid sample. Residuals from **a)** triexponential and **b)** 6 exponential model. Light grey lines correspond to the raw residuals. Black lines correspond to a low pass filtered (moving average, window size of 15 samples) residual signal.

We developed an algorithm to estimate the fraction of tissues within the hybrid signal through an iterative approach that minimizes the error between the measured signal and a synthetic signal based on an estimated ratio of constituent tissues.

A multiexponential fit **(3)** is performed on the hybrid signal to identify the relaxation times, $\boldsymbol{\tau}$, for the algorithm to utilize. A synthetic signal, $\hat{y}_{hy}(t, f)$, is produced as a linear combination of the MR signals from constituent tissues at a specified ratio:

$$\hat{y}_{hy}(t, f_{mu}) = f_{mu} * y_{mu}(t) + (1 - f_{mu}) * y_{fa}(t) \quad \textbf{(5)}$$

where f_{mu} indicates the fraction of the signal correspond to muscle, $y_{mu}(t)$ represents the acquired signal from pure muscle tissue, and $y_{fa}(t)$ represents the acquired signal from pure fat tissue. This signal is then fit **(4)** with the previously identified relaxation times to identify the amplitudes, $\boldsymbol{A}_{\boldsymbol{\tau}}^{pred}(f_{mu})$, corresponding to each relaxation time. Similarly, the amplitudes, $\boldsymbol{A}_{\boldsymbol{\tau}}^{meas}$, corresponding to the same relaxation times are found via a multiexponential fit **(4)** with the same previously identified relaxation times. The algorithm seeks to minimize the error between the amplitudes from the measured and synthetic by adjusting the ratio of constituent signals (i.e. pure muscle, pure fat) used to generate synthetic signal:

$$f_{mu}^{opt} = \underset{f_{mu}}{\operatorname{argmin}} \left\| \boldsymbol{A}_{\boldsymbol{\tau}}^{pred}(f_{mu}) - \boldsymbol{A}_{\boldsymbol{\tau}}^{meas} \right\|_2 \quad \textbf{(6)}$$

The error is minimized through the use of an iterative gradient descent algorithm. This technique could be extended towards more than two constituent signals.

This algorithm recovers the fractions of muscle and fat within the hybrid signal to within a 2% error (**Figure 7c**). This algorithm performs successfully despite the triexponential nature of each of the constituent signals.

Our algorithm allows for isolation and further analysis of a signal corresponding to a single tissue despite corruption of the acquired signal by another tissue with similar relaxation peaks. The acquired hybrid signal is unsuitable for standard exponential fitting based analysis methods due to the overlap of the constituent relaxation peaks. This problem is unique to inverse problems comprised of decaying exponentials due to their ill-posed nature *(21)*. We demonstrate this algorithm with multiexponential signals acquired from ex vivo fat and muscle tissue. This approach can be applied in other settings, such as estimating the change in relaxation properties of a single tissue due to a disease of pathology that causes a relaxation time shift within a tissue exhibiting a multiexponential MR signal.

This technique could be extended to consider multiple signals from each constituent tissue in order to improve its robustness, especially towards complex samples. Two measurements could be performed with different sensitivities towards spin diffusivity, for example, for each constituent tissue and for the hybrid sample. The addition of the second signal would increase the orthogonality of the basis signals, if the constituent samples have differences in diffusivity, and, therefore, may increase the accuracy and/or robustness of the technique in the presence of noise or other confounding signals. This same approach could also be applied with other pulse sequences (e.g. inversion recovery, saturation recovery, stimulated echoes, pulsed gradient echo, etc.) to take advantage of differences in T1, T2, and/or diffusivity in combination.

2.3. *RF Excitation Frequency*

The measurement depth of single-sided MR sensors, including our sensor based on the Unilateral Linear Halbach magnet array, is limited due to the rapid decay of the static magnetic field strength away from the surface of the sensor **(Figure 9)**.

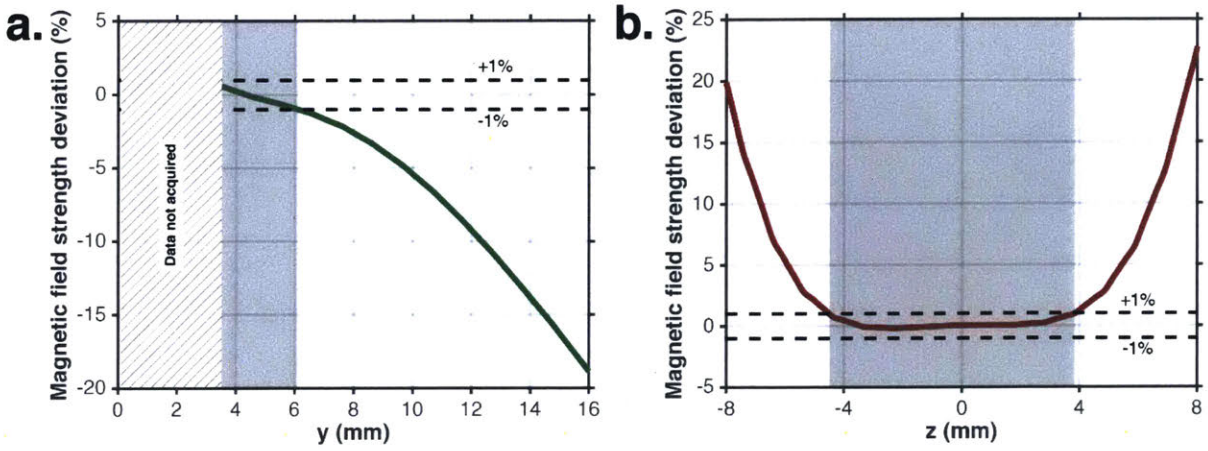

Figure 9. Static magnetic field profile characterization of portable MR sensor. Measured magnetic field strength deviation from B0 along **a)** y-axis and **b)** z-axis through the center of the uniform region. Shaded regions correspond to ±1% deviation from B0.

Our device is designed to perform a non-invasive scan of the skeletal muscle tissue within the lower leg of patients **(Figure 10a)**. These measurements are easily confounded by subcutaneous tissue despite selection of a measurement location with minimal subcutaneous thickness due to limitations in penetration depth *(20)*. A measurement technique localized towards the muscle tissue would allow isolation of the muscle signal from nearby confounding tissues.

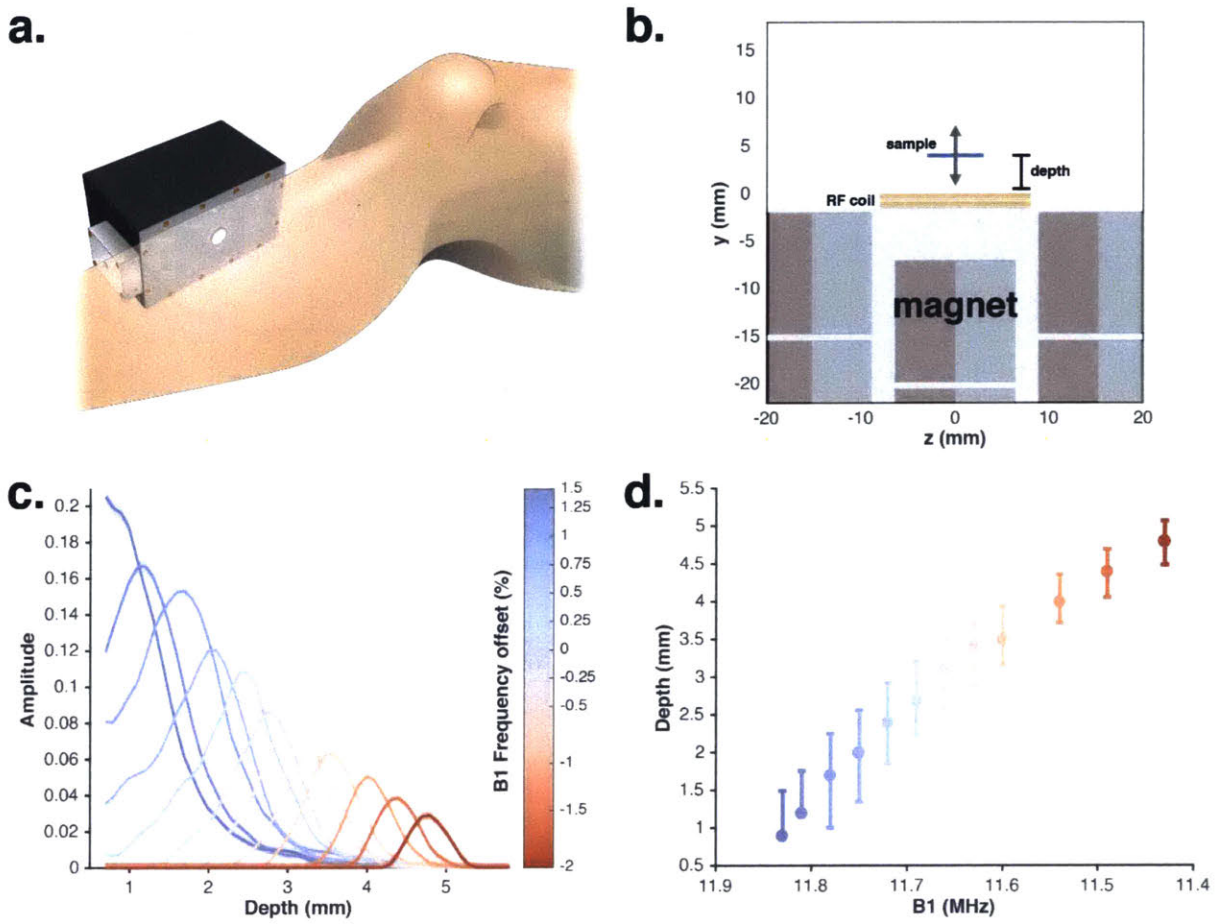

Figure 10. Sensitivity profile of portable MR sensor versus depth. a) Illustration of portable MR sensor adjacent to lower leg of human subject. **b)** Experimental schematic to characterize the sensitivity profile versus depth. **c)** The sensitivity of the sensor as a function of sample depth and RF excitation frequency shows that tuning the RF pulse frequency allows for adjustable sensitivity along the depth axis. Decreased B1 frequency enables deeper measurements remote from the surface of the sensor. Shaded regions indicate 95% confidence intervals of amplitude estimates. **d)** The projection of each curve onto the depth axis shows an RF pulse bandwidth of ~0.7% excites slices 0.6 to 1.3 mm thick with slice thickness decreasing further from the surface of the sensor. Circles indicate the depth of the peak of each sensitivity profile. Whiskers indicate slice thickness defined as full width at half maximum.

We show that tuning the RF excitation frequency of the portable MR sensor allows for spatial selection of the position of the sensitive region. We demonstrate this by measuring the sensitivity of the sensor towards a thin, planar sample as a function of both distance from the sensitive region and RF excitation frequency (B_1) **(Figure 10b)**.

A thin, planar sample was oriented parallel to the surface of the sensor and scanned along a line perpendicular to its surface. The sample consisted of a 380 µm × 6 mm × 6 mm pocket machined into PEEK (polyether ether ketone) stock filled with aqueous solution of a paramagnetic species (CuSO4). PEEK was used as it produced

a negligible MR signal. Measurements were performed with the center of the sample located between 0.690 mm and 6.59 mm from the surface of the sensor.

Measurements were performed with the CPMG pulse sequence with 2000 echoes, an echo time of 65 μs, a repetition time of 240 ms, a pulse duration of 12 μs, an acquisition bandwidth of 1 MHz (dwell time of 1 μs), and 16 acquired points per echo with a Kea2 spectrometer (Magritek, Wellington, New Zealand). The RF excitation frequency was varied across the following range (11.43, 11.49, 11.54, 11.6, 11.63, 11.66, 11.69, 11.72, 11.75, 11.78, 11.81, and 11.83 MHz) in order to identify changes in sensitivity as a function of RF excitation frequency. The amplitude in a triexponential fit **(4)** corresponding to the relaxation peak of the aqueous solution indicated the sensitivity of the sensor.

This sensitivity profile varies as a function of depth and exhibits a distinct region of peak sensitivity that is unique to each RF excitation frequency (Figure 10c). The use of smaller RF excitation frequencies enables localization of the measurement to regions located at a greater distance from the surface of the sensor. The effective slice thickness by a given RF excitation frequency decreases with distance from the sensor at a fixed excitation pulse bandwidth due to the increasing gradient of the static magnetic field **(Figure 10d)**. We show that an RF pulse bandwidth of 0.7% excites slices 0.6 to 1.3 mm thick with slice thickness decreasing with depth.

Tuning the RF excitation pulse frequency offers control over the fraction of proximal subcutaneous versus more distal muscle tissue in the acquired signal. This capability enables targeting of the measurement towards a tissue of interest.

2.4. *In Vitro Validation of RF Excitation Frequency*

The MR signal originating from the more distal muscle tissue is most relevant to the diagnosis of fluid disorders. The optimal measurement with our portable MR sensor would select an RF excitation frequency that sufficiently localizes the measurements towards the muscle tissue without unnecessarily sacrificing sensitivity. Smaller RF excitation frequencies enable increased measurement penetration depth at the expense of sensitivity **(Figure 10c)**. The optimal choice of RF excitation frequency should be informed by the local variation in subcutaneous thickness where regions with increased thickness will require a decreased frequency to achieve sufficient measurement penetration.

We demonstrate estimation of proximal subcutaneous tissue thickness with the portable MR sensor. We first fabricated synthetic tissue phantoms mimicking the relaxation properties of subcutaneous tissue and muscle tissue via aqueous solutions with varying concentrations of a paramagnetic species (CuSO4).

Synthetic tissue phantoms were fabricated from PEEK film (0.005-inch thickness) and nylon annular rings with an inner diameter of 6 mm and thickness of 1, 1.3, 1.5, and 3 mm with a tolerance of 0.3 mm. Each nylon ring was first bonded to a disk of PEEK film of identical outer diameter. The resultant cylindrical cavity was filled with fluid mimicking the MR relaxation properties of subcutaneous fat (i.e. soybean oil, $CuSO_4$). Then a second disk of PEEK film was used to seal each phantom.

Portable MR sensor measurements were performed with the CPMG pulse sequence with the following parameters common to all scans: 8192 echoes, 1 dummy echo, an echo time of 65 µs, a measurement time of 1065 ms, a repetition time of 1517 ms, a pulse duration of 12 µs, an acquisition bandwidth of 1 MHz (dwell time of 1 µs), and 16 acquired points per echo. RF excitation frequencies of 11.43, 11.53, 11.58, 11.66, 11.73, and 11.83 MHz were acquired.

The muscle fraction, $f_{mu}^{meas}(B_1)$, was estimated at each RF excitation frequency, B_1, for each phantom thickness from these measured signals using the previously described algorithm. The relaxation times used for each tissue were derived from monoexponential fits on the synthetic subcutaneous and muscle tissue solutions used within the synthetic tissue phantoms. Muscle fraction, $f_{mu}^{pred}(B_1, z)$, was similarly derived from the depth sensitivity profile data, $A(B_1, z)$, for each RF excitation frequency given a guess of the phantom thickness, z:

$$f_{mu}^{pred}(B_1, z) = \frac{\int_z^{\infty} A(B_1, z)dz}{\int_0^{\infty} A(B_1, z)dz} \tag{7}$$

The thickness of the synthetic fat layer, z^{opt}, was estimated by minimizing the error between the estimated muscle fraction derived from the measured data and the predicted muscle fraction derived from the depth sensitivity profile data:

$$z^{opt} = \underset{z}{\operatorname{argmin}} \left\| f_{mu}^{meas}(B_1) - f_{mu}^{pred}(B_1, z) \right\|_2 \tag{8}$$

The phantoms were designed to fully span the sensitive region of the sensor **(Figure 11a)**. The relaxation times of the synthetic subcutaneous tissue phantom were similar to that of ex vivo tissue while allowing for precise control over sample geometry **(Figure 11b)**.

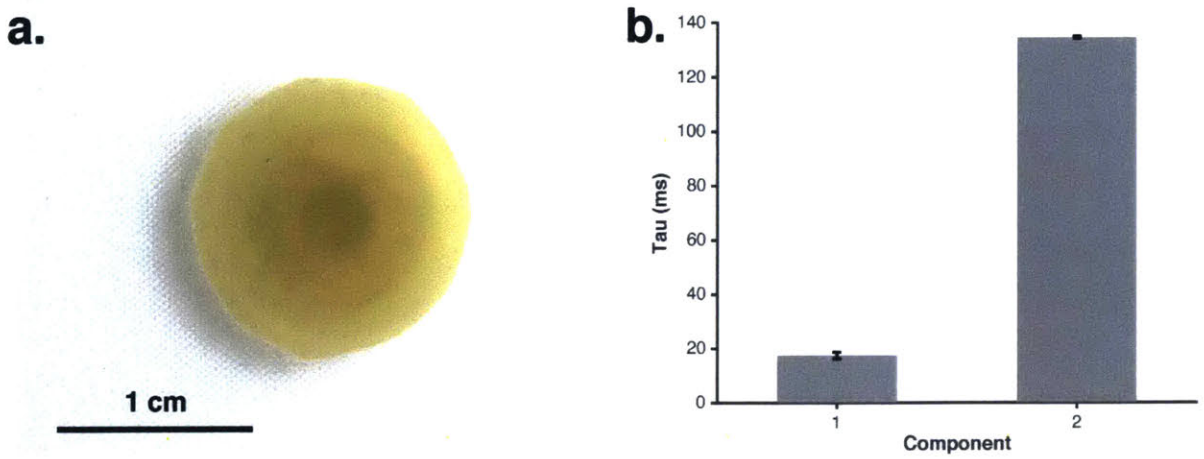

Figure 11. Synthetic subcutaneous tissue phantom. a) Photograph of phantom shows soybean oil cavity surrounded by a PEEK housing. **b)** A biexponential fit of CPMG signal of soybean oil acquired on portable MR sensor produces two distinct relaxation times. Error bars represent 95% confidence intervals on relaxation time estimates.

The phantoms were then arranged with the subcutaneous tissue directly in contact with the RF coil of the portable MR sensor and the muscle tissue placed against the subcutaneous tissue phantom **(Figure 12a)**. The thickness of the subcutaneous tissue was varied (1, 1.3, 1.5, and 3 mm) to mimic natural variability both within and between patients. We measured each configuration of phantoms with the CPMG pulse sequence with six unique RF excitation frequencies.

Simulations were performed to identify the necessary signal to noise ratio (SNR) to accuracy estimate the muscle fraction from a heterogeneous signal **(Figure 13)**. Muscle to fat ratios of 20:80, 50:50, and 80:20 were considered. Signal to noise ratios of each constituent signal (i.e. muscle, fat) of 25, 50, 75, 100, 125, 150, 175, 200, 225, and 250 were considered for a total of 100 pairwise combinations of signal to noise ratios. For each pair of SNRs at each muscle to fat ratio, a synthetic muscle and fat signal at the corresponding SNR was generated based on the relaxation times and amplitudes observed in triexponential fits **(4)** of ex vivo measurements of isolated tissue. A resultant hybrid signal was created as the sum of these two signals. The muscle to fat ratio was estimated using the previously described algorithm **(6)**. Error was computed as the absolute difference of this estimate from the true muscle to fat ratio. 120 trials were performed for each combination of SNRs and muscle to fat ratios. The results of this simulation guided measurements of phantoms.

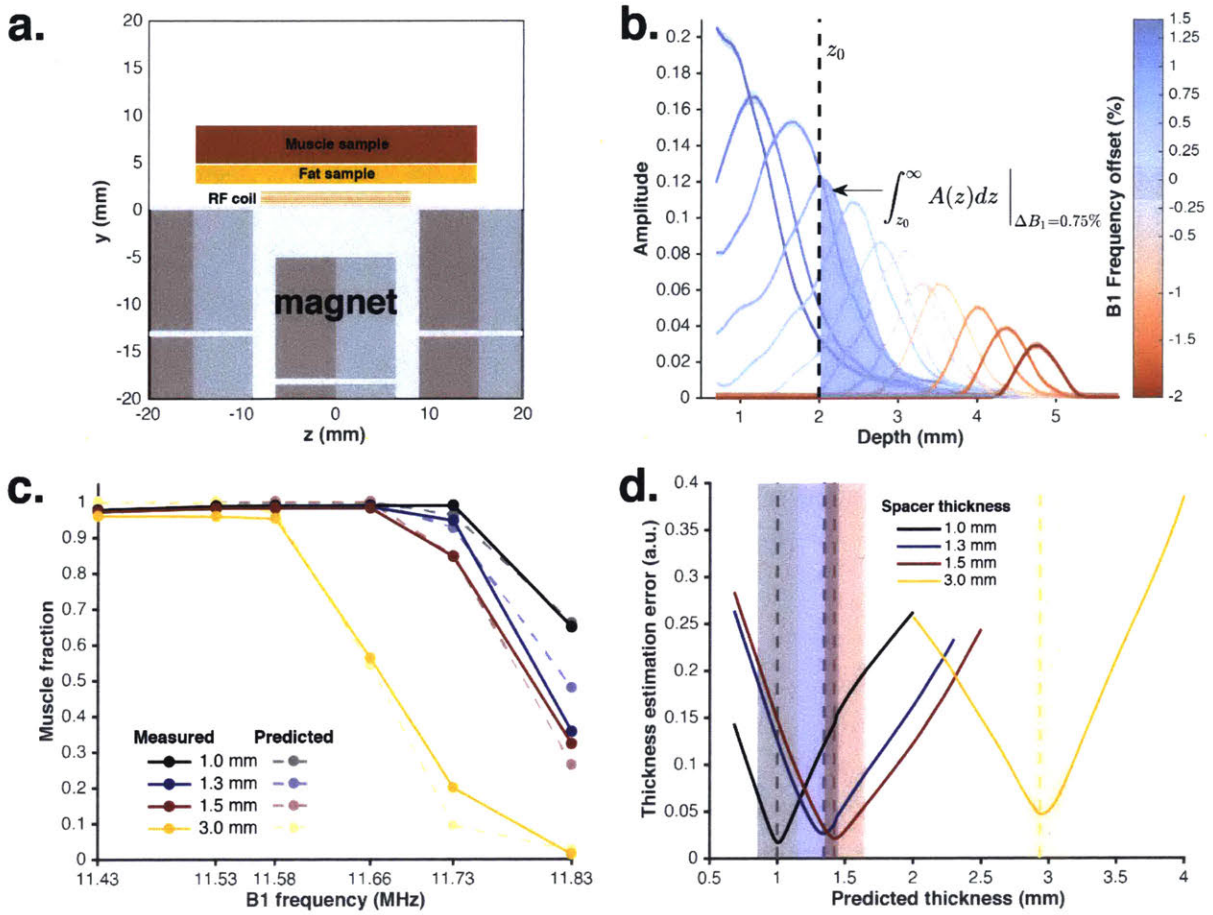

Figure 12. Estimation of proximal subcutaneous tissue thickness. a) Experimental schematic identifying planar subcutaneous and muscle tissue samples on top of portable MR sensor. **b)** A schematic illustrating the use of the depth sensitivity profiles to estimate the thickness of a tissue layer. **c)** Experimentally measured and predicted muscle signal fractions from each unique subcutaneous tissue thickness versus RF excitation frequency. **d)** Thickness estimation error versus predicted thickness for each unique subcutaneous tissue thickness. Dotted lines indicate the estimated synthetic tissue thickness, corresponding to the minima of each error curve. Shaded regions indicate 0.3 mm uncertainty in the true thickness of each subcutaneous tissue layer.

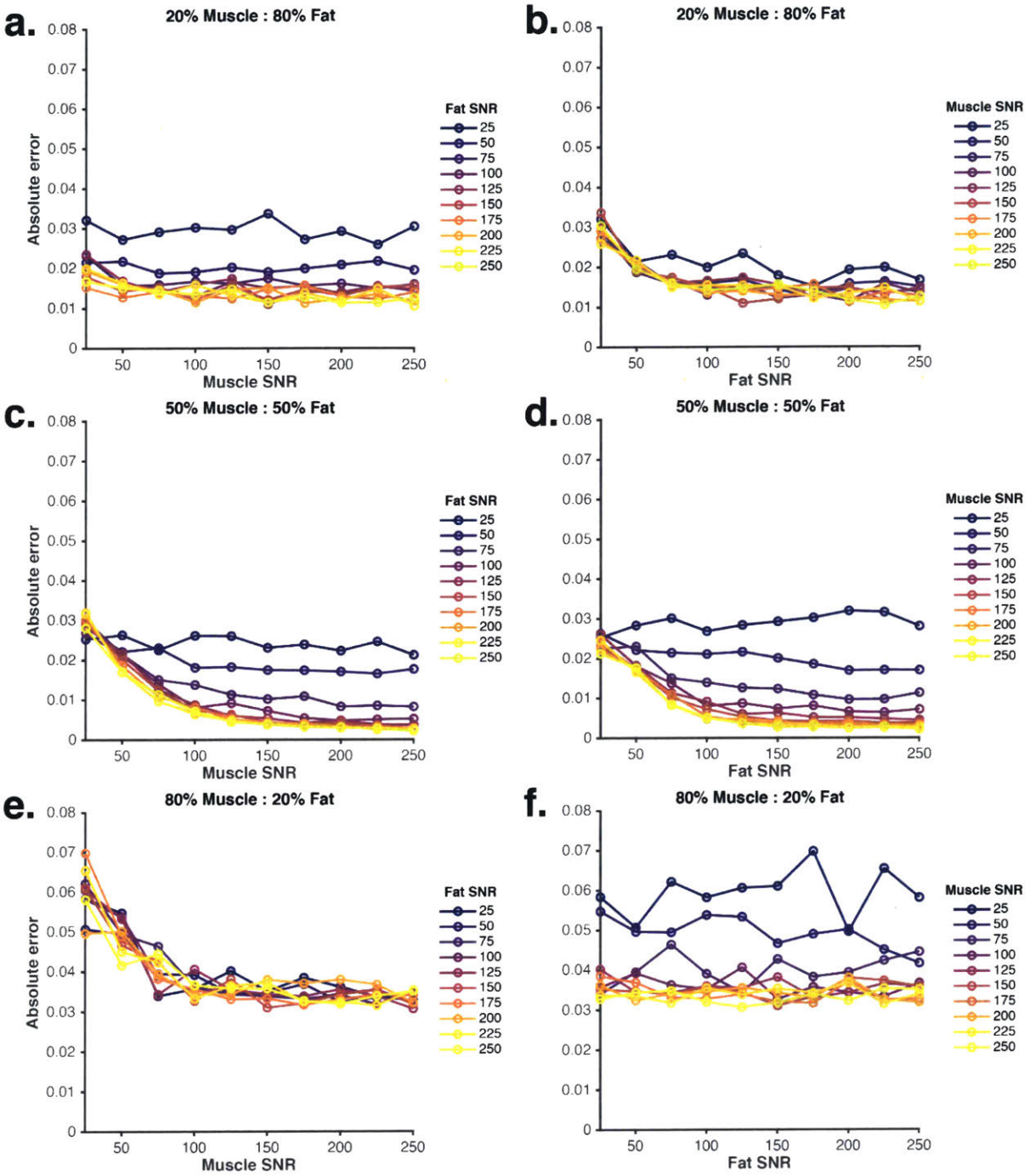

Figure 13. Simulation of error in estimating muscle and fat fractions versus signal SNR. Simulations were performed at three muscle to fat ratios: **a-b)** 20:80, **c-d)** 50:50, **e-f)** 80:20.

The expected signal amplitude originating from the distal muscle tissue for a given subcutaneous thickness (e.g. 2 mm) can be estimated as the integral of the sensor sensitivity profile taken across the expected depth of the muscle tissue (e.g. greater than 2 mm) for each RF excitation frequency **(Figure 12b)**. This can be converted to an estimate of the muscle tissue fraction by dividing it by the integral of the

entire sensitivity profile at the given RF excitation frequency. This technique can be used to precisely quantify subcutaneous tissue thickness from measurements of a muscle sample with a more proximal layer of subcutaneous tissue. Estimates of muscle fraction from experimentally acquired signals show strong agreement with estimated muscle fractions for the same subcutaneous thickness across a wide range of RF excitation frequencies **(Figure 12c)**.

Sensor sensitivity as a function of depth can be used for precise estimation of the thickness of the subcutaneous tissue. The muscle fractions generated by integrating the sensitivity profiles for a candidate thickness can be compared with muscle fractions from experimentally acquired signals. We then identify the optimal candidate thickness by minimizing the error between muscle fraction estimates and those from the measured signal. This optimal thickness represents the actual thickness of each phantom **(Figure 12d)**. Estimation of phantom thickness using this approach is accurate to within 0.1 mm, which is smaller than the tolerance on the construction of the phantoms (0.3 mm).

An algorithm to perform acquisition at the optimal RF excitation frequency could be implemented by utilizing this method. The optimal RF excitation frequency would be sufficiently low as to ensure a significant fraction of the sensitive region is located within the target tissue without being so low as to unnecessarily sacrifice sensitivity. This optimal frequency would be dependent on the subcutaneous tissue thickness, geometry of the portable MR sensor, and pulse parameters (e.g. excitation pulse bandwidth). Estimation of the optimal RF excitation frequency is made more robust and accurate by performing measurements of a tissue geometry at multiple RF excitation frequencies.

2.5. *Diffusion Weighting*

Distinct tissues can have very similar relaxation properties (e.g. times and amplitudes) making identification and further characterization of changes in relaxation properties difficult *(22–24)*. Measurements of relaxation properties via CPMG are inherently affected by the diffusivity of spins (e.g. water in tissue) within the sample *(25)*. Here we demonstrate that explicitly manipulating the echo time within CPMG allows control over the effect of diffusivity on the relaxation properties of the signal with our portable MR sensor.

Varying the echo time between excitation and subsequent refocusing pulses provides control over the magnitude of signal attenuation induced by sample diffusivity *(25)*. Signal attenuation between sequential refocusing pulses in CPMG

is driven by both T2 decay and the motion of spins within the magnetic field. The T2 decay term is proportional to the echo time while the diffusion term is proportional to the echo time cubed. Therefore, by controlling the echo time, the relative signal attenuation due to each factor can be varied.

Four aqueous solutions of polyethylene glycol (PEG) and gadolinium are prepared with identical T2 relaxation time and distinct diffusion coefficients. Samples consisted of aqueous solutions of varying concentrations of gadolinium trichloride (Gd) and polyethylene glycol (PEG) (mw: 4000 g/mol). Four samples (A, B, C, and D) were prepared with 126, 57, 28.5, and 0.17 mM of PEG and 0.42, 0.5, 0.5, and 0.5 mM of Gd, respectively. The relaxation data from the benchtop NMR spectrometer were acquired via CPMG with 25000 echoes, an echo time of 100 µs, a repetition time of 60 seconds, an RF excitation frequency of 19.95 MHz, an excitation pulse duration of 1.9 µs, an inversion pulse duration of 3.8 µs, an acquisition bandwidth of 1 MHz (dwell time of 3 µs), and 1 acquired point per echo with a (minispec mq20, Bruker, USA). The diffusion NMR data was acquired from a Bruker Avance III HD 400 NMR spectrometer with a pulsed gradient spin echo pulse sequence. Estimation of diffusivity was performed with MestReNova v12.0.4 (Mestrelab Software S.L.). The data from the portable MR sensor were acquired with the CPMG pulse sequence with the following parameters all measurements: a measurement time of 1.065 sec, an RF excitation frequency of 11.66 MHz, a repetition time of 452 ms, a pulse duration of 12 µs, an acquisition bandwidth of 1 MHz (dwell time of 1 µs), and 16 acquired points per echo. Echo times of 206, 223, 260, 368, 520, 735, and 1040 µs were utilized. All relaxation times were extracted by fitting the decay curves with a monoexponential model **(3)**.

PEG concentration primarily affected the diffusivity of water while gadolinium primarily affected relaxation properties. T2 relaxation times were estimated via measurements on a benchtop NMR spectrometer via CPMG. The time domain signals and T2 relaxation times, estimated via a monoexponential fit, were nearly identical across all samples **(Figure 14a-b)**. The diffusivity of water within the samples, estimated via pulsed gradient spin echo pulse sequence on a Bruker NMR spectrometer, varies significantly with PEG concentration **(Figure 14c)**.

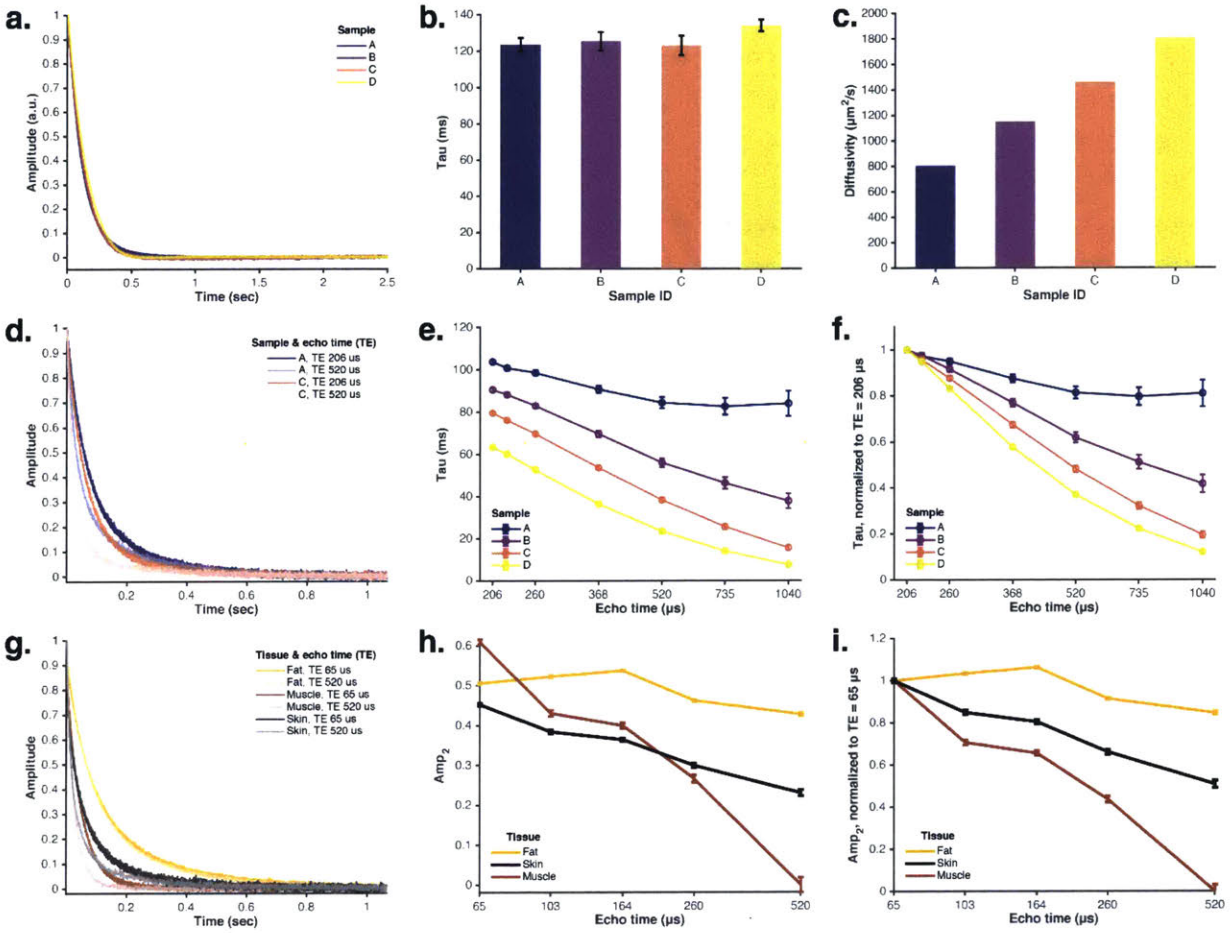

Figure 14. Varying echo time provides portable MR sensor with sensitivity towards sample diffusivity. a) Time domain decay curves and **b)** extracted relaxation times from measurement of samples with distinct diffusivities acquired with CPMG on benchtop NMR spectrometer. Error bars represent 95% confidence intervals on relaxation time estimates. **c)** Diffusivity estimated via pulsed gradient spin echo measurements of these samples with an NMR spectrometer. **d)** Time domain decay curves, **e)** relaxation times, and **f)** relaxation times normalized to the relaxation time at TE = 206 μs from measurements of these samples on portable MR sensor with CPMG with varying echo time. Error bars represent 95% confidence intervals on the relaxation time estimates. **g)** time domain CPMG decay curves of ex vivo tissue measured with portable MR sensor at two echo times. **h)** Slow amplitude (amp2) and i) slow amplitude normalized to slow amplitude at TE = 65 μs of a biexponential fit on these measurements. Error bars represent 95% confidence intervals on amplitude.

Measurements of the aqueous solutions were performed with CPMG with varying echo time with the portable MR sensor **(Figure 14d-f).** The change in decay rate in the time domain **(Figure 14d)** and estimated relaxation time extracted from a monoexponential fit **(3) (Figure 14e)** of each sample differs as a function of echo time. Increased echo time leads to a decrease in relaxation time. The magnitude of this decrease is more pronounced with increased sample diffusivity. The relative change in relaxation time as a function of echo time clearly stratifies samples by diffusivity **(Figure 14f)**. For example, the sample with the highest diffusivity

exhibits an 88% decrease in relaxation time while the sample with the lower diffusivity exhibits only a 19% decrease in relaxation time between the fastest and slowest echo time acquired.

We then measured three distinct *ex vivo* tissues on the portable MR sensor to demonstrate that this technique is capable of identifying differences in diffusivity within complex samples producing multiexponential signals. Tissues were extracted from a rat identically to as previous described. Each tissue was measured with the portable MR sensor with the CPMG pulse sequence with an RF excitation frequency of 11.60 MHz, a repetition time of 1517 ms, a measurement time of 1.065 sec, a pulse duration of 12 μs, an acquisition bandwidth of 1 MHz (dwell time of 1 μs), and 16 acquired points per echo. Echo times of 65, 103, 164, 260, and 520 μs were used in order to identify changes in estimated relaxation time as a function of echo time. First, the signals from each tissue across all echo times were summed and fit with a biexponential model **(3)**. to identify average two component relaxation times for each tissue. Then for each tissue, each signal at each echo time was fit with a biexponential model **(4)** with the respective relaxation times corresponding to the tissue. This allowed differences between signals to be identified as changes in the relative amplitudes of the slow versus fast relaxation peaks.

Fat, skeletal muscle, and skin are excised from a rat and measured with CPMG with varying echo times. The change in decay rate of each signal is dependent on echo time **(Figure 14g)**. We then performed a biexponential fit to identify the effect of varying echo time on the amplitude corresponding to the slower, more highly diffusive fluid compartment of each tissue. The second amplitude from the biexponential fit of the muscle signal decreases more quickly with echo time than that of the skin or fat signals **(Figure 14h)**. This shows that the relative diffusivity of water within the slow component of muscle is greater than that of skin and fat *(26–28)*. Furthermore, the relative change in this amplitude as a function of echo time clearly stratifies each tissue which allows for straightforward identification of each tissue despite similarities in relaxation properties **(Figure 14i)**.

We demonstrate sensitivity towards diffusivity with the portable MR sensor by taking advantage of its highly inhomogeneous static magnetic field. This measurement is performed by varying the echo time which serves a similar purpose as the switchable gradient fields found in more traditional implementations of diffusion-weighted pulse sequences. The relatively high static magnetic field inhomogeneity, a characteristic of most single-sided MR sensors, enables strong diffusion weighting to be achieved with relatively short echo times. The dependency of relaxation time on both echo time and sample diffusivity can be used to identify the T2 and diffusivity of a sample.

3 Chapter 3: *In Vivo* Validation

Chapter 3 presents *in vivo* validation of the methods discussed in Chapter 2. A rodent model of acute muscle edema demonstrates utility of multicomponent T2 relaxometry, RF excitation frequency selection, and diffusion weighting. Data presented in this chapter was collected, analyzed, and described in collaboration with Ashvin Bashyam.

3.1. *Clinical Motivation*

A portable and non-invasive sensor of tissue fluid distribution would aid in the diagnosis of disorders of fluid volume status and inform therapeutic decisions across a wide range of patient populations. The inability to maintain normal fluid volume status can indicate the progression of a variety of diseases. Fluid overload (hypervolemia) is associated with end-stage renal disease (ESRD), congestive heart failure (CHF), and liver failure *(6,14,29–35)*. Identification of fluid overload may inform improved treatment for patients with these chronic diseases.

Accurate, real-time monitoring of volume status would improve outcomes for ESRD patients *(34)*. ESRD patients have excess fluid regularly removed via hemodialysis (HD). Ultrafiltration goals during HD are guided by estimated euvolemic weight (i.e. dry weight) of the patient. The removal of excess fluid beyond that necessary to reach dry weight leads to intradialytic hypotension (IDH). IDH occurs in up to 75% of hemodialysis patients and can cause nausea, vomiting, cramping, and chest pain *(36)*. This negatively affects patient quality of life and reduces long-term compliance with HD prescription *(4)*. Furthermore, IDH is associated with increased two-year mortality and morbidity in the form of bowel ischemia, stroke, fistula thrombosis, and myocardial infarction *(4,6,37)*. There currently exists no reliable, robust indication of when HD patients are at risk for IDH *(6,14,34)*.

Current techniques for the identification and treatment of fluid overload are unable to provide a valid assessment of volume status consistent across HD sessions and HD patients *(14,32–34,38)*. Existing management efforts rely heavily on clinical signs and patients' weight change throughout the course of a HD session *(33)*. These techniques do not resolve individual fluid compartments and are easily confounded by changes in nutrition, lean body mass, diet, and many other factors *(15,32,39)*. Alternative techniques for indicating a patient's dry weight, such as bioimpedance, blood pressure, and biochemical markers similarly rely on systemic physiological changes and therefore exhibit large interpatient and intrapatient variability *(13,14,40)*.

Disruptions in fluid volume status are characterized by changes in the distribution of water between body fluid compartments and tissues *(41–43)*. Hypovolemia and hypervolemia induce respective depletion and expansion of the intramuscular fluid compartments (extracellular and intracellular). Furthermore, the intramuscular extracellular fluid (ECF) compartment is more highly responsive to these fluid shifts than the intracellular fluid (ICF) compartment and either compartment in the subcutaneous space *(42,44)*. Therefore, a localized measurement of shifts in fluid within the intramuscular fluid compartments could serve as an indicator of disruption to systemic euvolemia.

Magnetic resonance measurements of distinct fluid compartments have demonstrated sensitivity to both local and systemic shifts in tissue fluid distribution *(3,44–47)*. We previously conducted a clinical study in ESRD patients undergoing HD to assess the ability of MR measurements localized to the skeletal muscle to identify changes in fluid volume status. This study showed that the change in amplitude of the multicomponent T2-based signal corresponding to intramuscular ECF in a localized measurement can identify systemic fluid imbalances *(44)*. We further corroborated these findings in a rodent model of fluid depletion and demonstrated sensitivity towards weight loss via both systemic and localized measurements *(47)*. MRI is impractical for use as a routine clinical diagnostic due to its resource intensiveness, high cost, long acquisition time, and lack of portability. Portable MR sensors have exhibited sensitivity towards fluid distribution in tissues, including the muscle, in both animal and human studies *(44,47)*. This resolves many of the limitations of MRI by providing a portable, low-cost, high sensitivity platform to perform MR measurements. In our prior clinical study, the portable MR sensor was unable to reproduce absolute measurements of fluid volume status as seen on the MRI of skeletal muscle due to the highly variable subcutaneous tissue thickness between patients *(44)*.

Portable MR devices, often realized via single-sided magnets, can be inadequate in their ability to isolate the measurement towards the muscle tissue due to limitations in penetration depth, spatial selectivity, and available contrast mechanisms *(48,49)*. Measurement of skeletal muscle tissue in the extremities requires penetration beyond the proximal subcutaneous tissue *(20)*. Measurement depth is highly constrained due to the rapid attenuation of static and RF magnetic fields away from the surface of the sensor. Larger devices can achieve increased penetration depth, but this compromises portability and increases cost. Encoding spatial information via switchable gradients is substantially more difficult with single-sided MR sensors compared to MRI due to the high field inhomogeneity of their static and gradient magnetic fields and restrictions on allowable tissue RF power deposition. Therefore, single-sided MR measurements of the muscle are often

contaminated by other nearby tissues. The available contrast mechanisms to help isolate the signal from a single tissue (i.e. muscle) are restricted due to the relatively low sensitivity and high magnetic field inhomogeneity of single-sided MR devices. Many pulse sequences capable of separating fat from other tissues rely on phenomena such as chemical shift, which cannot be realized given the high field inhomogeneity of single-sided MR sensors.

The presence of confounding tissues, such as subcutaneous tissue, can obscure or confound measurements intended to be isolated towards the muscle tissue. Separation of signals originating from tissues with similar relaxation properties is difficult and a substantial source of error in relaxometry studies *(24)*. Performing multicomponent T2 measurements relatively deep within the tissue with a single-sided MR sensor while maintaining sensitivity is challenging.

We demonstrate a single-sided MR sensor based on the Unilateral Linear Halbach magnet design capable of identifying intramuscular fluid shifts via a localized measurement. This sensor is capable of performing depth-resolved measurements by tuning the RF excitation frequency. We demonstrate quantification of the relative fractions of tissues within heterogeneous samples via multicomponent T2 relaxometry. The sensor exhibits contrast dependent on the diffusivity of the sample. We leverage this capability to isolate and characterize tissues with otherwise similar MR relaxation properties. We then apply these techniques in combination to show that a depth-resolved, diffusion-weighted, multicomponent T2 relaxometry measurement can identify and track the onset and progression of muscle edema despite the presence of a confounding proximal subcutaneous tissue layer.

We primarily utilize a portable MR sensor realized through the use of a Unilateral Linear Halbach magnet geometry *(17)*. Briefly, this sensor consists of an array of 180 permanent magnets arranged to produce a static magnetic field (0.28 Tesla) with <2% field variation over a volume spanning approximately 12 x 6 x 6 mm. Bashyam et al. provides detailed descriptions of the design, construction, and characterization of the MR sensor *(47)*.

These innovations enable miniaturized, single-sided MR sensors to perform measurements of fluid distribution in the muscle tissue, the tissue that is most responsive to disruptions in fluid volume status. This non-invasive, portable, point of care technique has the potential to help diagnose and manage conditions involving disruptions in fluid distribution such as congestive heart failure, end-stage renal disease, and dehydration.

3.2. *Muscle Edema*

We induced acute, focal muscle edema to expand the intramuscular interstitial fluid compartment via injection of λ-carrageenan into the biceps femoris muscle in the lower leg of a rat. Acute muscle edema was induced via an injection of 200 µL of 1% λ-carrageenan solution into the biceps femoris of the lower hind leg of a 400 g, male Sprague-Dawley rat. Injections were performed with a 26 gauge needle with the tip of the needle inserted perpendicularly and approximately 4 mm into the skin. The injection was performed at an approximate flow rate of 10 µL/sec. The needle was held in place for approximately 30 seconds before removing it from the leg to reduce backflow and bleeding. Rats were administered 1 mg/kg of Buprenorphine SR via thoracic subcutaneous injection immediately prior to injection to minimize discomfort. Rats were anesthetized with 2% isoflurane during the injection. We confirmed the presence of muscle edema via hematoxylin and eosin (H&E) staining of muscle tissue adjacent to the site of injection **(Figure 15a-b)**. We confirmed the presence of muscle edema via hematoxylin and eosin (H&E) staining of muscle tissue adjacent to the site of injection **(Figure 15c)** and after **(Figure 15d)** injection.

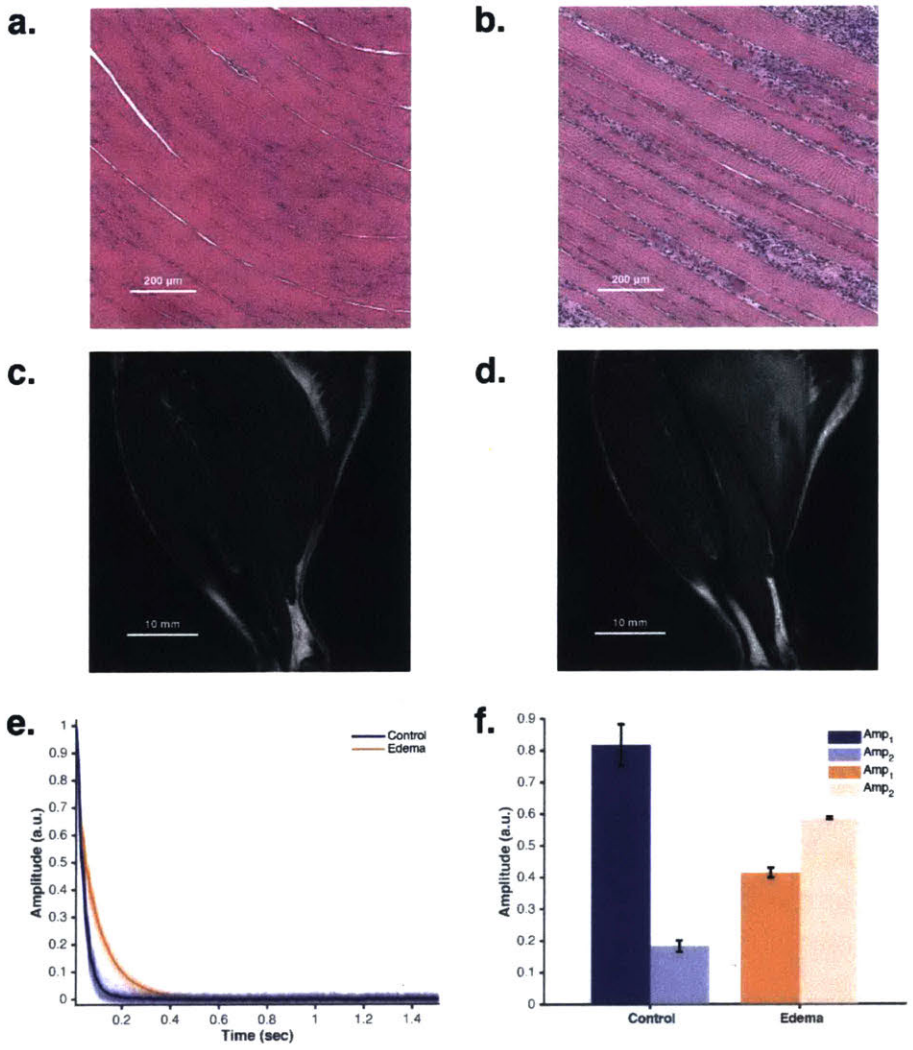

Figure 15. Intramuscular muscle edema shifts multicomponent T2 relaxometry signal. a-b) H&E stains of biceps femoris muscle **(a)** before and **(b)** after intramuscular injection of λ-carrageenan shows acute inflammation and interstitial expansion. **c-d)** T2 weighted MRI images of rat lower leg **(c)** before and **(d)** after onset of acute muscle edema. **e)** Decay curves from T2 relaxometry acquired via MRI before and after onset of muscle edema show a difference in decay rate. Shaded regions indicate variance in signal generated through bootstrapping. **f)** Relative amplitudes of biexponential fits **(4)** on control and edema echoes. Relaxation times are derived from a biexponential fit **(3)** on the mean of all echoes.

For H&E histology, biceps femoris muscle tissue was excised from a freshly euthanized rat and fixed in formalin for 24 hours at 4 C° and stored in 70% ethanol until paraffin-embedding, sectioning, and staining.

MRI scans were performed with a 7T/310/ASR (Agilent, formerly Varian) scanner with vnmrj software (version 3.2b), equipped with a 63mm/108mm quadrature birdcage coil. Rats were first anesthetized with 2% isoflurane, then oriented in a supine position, and maintained on 1-2% isoflurane throughout data collection.

Warm air (37 C) was delivered to maintain body temperature of animals. T2 weighted anatomical scans were performed with FSEMS (fast spin echo multi slice) with repetition time 2000 ms, echo time 20 ms, echo train length 4, kzero 2, 2 averages, 2 dummy scans, 256 x 256 acquisition matrix, 40 x 40 mm field of view, and 1 mm slice thickness. A series of spin echo images for T2 relaxometry were acquired with MEMS (multi echo multi slice) with TR 7600 ms, TE 10 ms, 151 echoes, 4 averages, 64 x 32 x 5 acquisition matrix, 40 x 40 mm field of view, and 1 mm slice thickness. Slice acquisition order was interleaved using standard two-pass interleaving. All images were acquired along the sagittal plane of the animal.

The MRI data are acquired as magnitude images; therefore, the noise distribution is best approximated as a Rician distribution. We transform the noise distribution of each multi-echo signal from Rician to Gaussian by iteratively estimating the variance of the noise, extracting an estimate of the contribution from noise to each echo, then mapping between the cumulative distribution functions of a Rician distribution to a Gaussian distribution *(50,51)*. The noise variance is estimated iteratively until the absolute value of the median of the echo magnitude in the noise tail is minimized.

The region of hyperintensity in the biceps femoris muscle, visible in the image 24 hours after injection, indicates fluid accumulation in the interstitial space **(Figure 15d)**. A series of spin echo MRI images were acquired to provide a T2 decay curve for quantitative characterization of muscle edema **(Figure 15e-f)**. Composite T2 decay signals formed from voxels corresponding to muscle tissue indicate an increase in decay time from before to 24 hours after injection **(Figure 15e)**. A biexponential fit demonstrates an increase in signal amplitude corresponding to the intramuscular ECF **(Figure 15f)**.

We show that the portable MR sensor can identify changes in intramuscular fluid distribution despite the presence of a confounding signal from proximal subcutaneous tissue. We achieved this by localizing the signal via tuning of the RF excitation frequency and by isolating the muscle signal via diffusion-weighted measurements and T2 multicomponent relaxometry.

The hind leg of the rat was placed on top of the RF transceiver coil of the portable MR sensor **(Figure 16c)**. A synthetic subcutaneous tissue phantom, located between the sensor and the rat leg, simulated the presence of a substantial subcutaneous tissue layer. The subcutaneous tissue phantom consisted of a cylindrical volume of soybean oil enclosed in a thin plastic housing **(Figure 11a)**. The subcutaneous tissue phantom appears as a biexponential signal when

measured with the portable MR sensor with relaxation times of 58 and 226 ms **(Figure 11b)**.

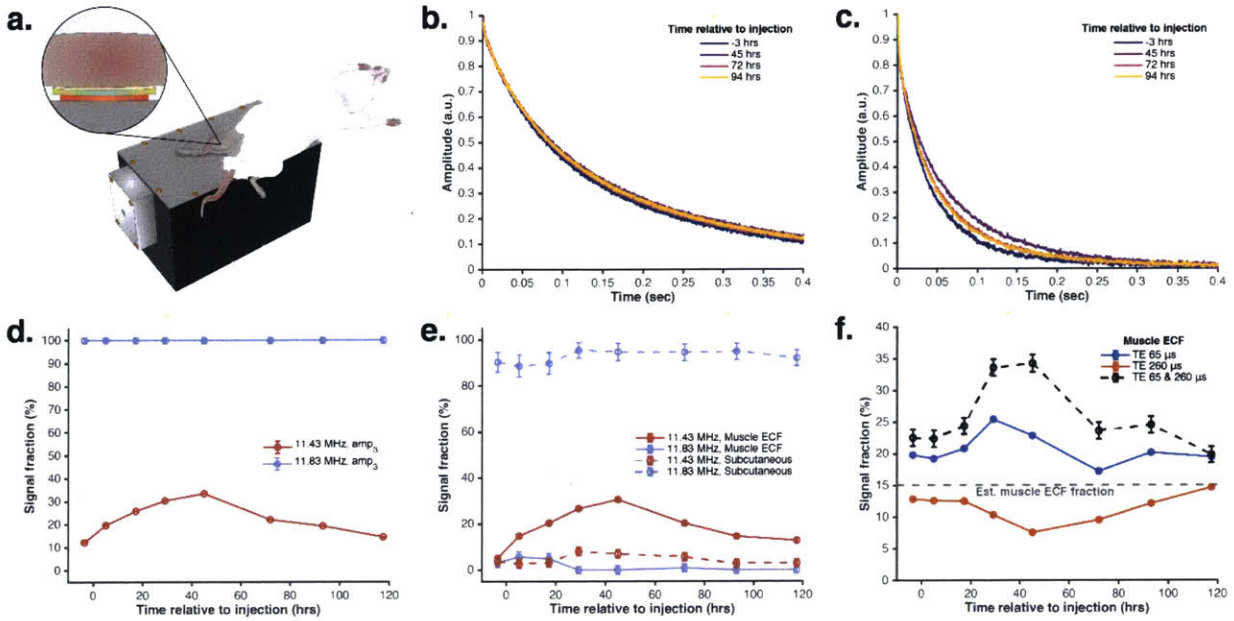

Figure 16. Portable MR sensor identifies onset and recovery of acute muscle edema. a) Illustration of portable MR sensor with synthetic subcutaneous tissue phantom placed between RF transceiver coil and rat lower leg. **b-c)** Time domain decay curves from portable MR measurement of rat leg at an RF excitation frequency of **b)** 11.83 MHz and **c)** 11.43 MHz. **d)** Slow amplitude of triexponential fit on 11.43 MHz and 11.83 MHz measurements. **e)** Amplitude attributed to muscle ECF and subcutaneous signal from a five exponential fit on 11.43 MHz and 11.83 MHz measurements. **f)** Amplitude attributed to muscle ECF from 11.60 MHz measurements at echo times of 65 µs (blue) and 260 µs (orange). Black dashed line indicates estimated muscle edema derived from both measurements. All error bars indicate 95% confidence intervals on amplitude estimates.

MR measurements were performed before injection and longitudinally at regular intervals for a total period of 121 hours. Anesthetized (2% isoflurane) rats were placed on top of the portable MR sensor in a supine position. The lower leg was positioned on top of the RF coil and secured with tape to minimize motion during signal acquisition. A synthetic subcutaneous tissue phantom was located between the sensor and the rat leg. The phantom consisted of a 2 mm thick cylindrical volume of soybean oil enclosed in a thin PEEK housing, Four measurements were performed with the CPMG pulse sequence with following parameters common to all scans: a repetition time of 1517 ms, a measurement time of 1065 ms, a pulse duration of 12 µs, an acquisition bandwidth of 1 MHz (dwell time of 1 µs), and 16 acquired points per echo. The first, second, third and fourth scans were performed with an RF excitation frequency of 11.43 MHz, 11.60 MHz, 11.60 MHz, and 11.83 MHz, respectively. The first, second, and fourth scans were performed with an echo time of 65 µs, 8192 echoes, and 1 dummy echo. The third scan was performed with

an echo time of 260 μs, 4096 echoes, and 0 dummy echoes. These four measurements were repeated at -4, 5, 17, 29, 45, 72, 93, and 117 hours relative to the time of injection for a total of eight time points.

The 11.43 MHz and 11.83 MHz signals at each time point were fit with a triexponential model **(4)** with the relaxation times set to that of muscle tissue. The slowest component was attributed to the extracellular fluid within the muscle tissue **(Figure 16f)**. The same two signals at each time point were then fit with a five component model **(4)** with the relaxation times set to that of both muscle tissue and subcutaneous tissue. The amplitudes of the two components corresponding to the subcutaneous tissue were summed and attributed to the subcutaneous tissue. The slowest remaining component was attributed to the extracellular fluid within the muscle tissue **(Figure 16e)**.

In order to estimate the degree of diffusion attenuation, Δ, a baseline value, $A_{260\mu s}^{baseline}$, for muscle ECF fraction in the 11.60 MHz 260 μs signal is first established. The deviation from this baseline of the muscle ECF amplitude of the 11.60 MHz 260 μs signal, $A_{260\mu s}$, is used to establish an estimate of the signal attenuation due to increased diffusivity of the muscle ECF:

$$\Delta = \frac{A_{260\mu s}^{baseline} - A_{260\mu s}}{A_{260\mu s}^{baseline}} \quad \textbf{(9)}$$

This estimate of increased diffusivity is used to enhance the muscle ECF amplitude from the 11.60 MHz 65 μs signal. The relative decrease in the signal is used to scale the muscle ECF amplitude of the 11.60 MHz 65 μs signal **(Figure 15h)** to produce an adjusted estimate of the muscle ECF amplitude, $A_{65\mu s}^{adj}$:

$$A_{65\mu s}^{adj} = A_{65\mu s} * (1 + \Delta) \quad \textbf{(10)}$$

The first set of MR measurements demonstrates the utility of achieving target localization via tuning RF excitation frequency. A series of MR measurements acquired at a high RF excitation frequency (11.83 MHz) are unable to resolve changes in the signal originating from the muscle tissue as the signal is largely localized towards the proximal subcutaneous tissue **(Figure 16b)**. Identical measurements performed at a lower RF excitation frequency (11.43 MHz) clearly identify an increase in decay rate associated with onset of muscle edema, followed by a reversion towards the baseline signal **(Figure 16c)**.

A triexponential fit **(3)** was performed on the sum of these signals to identify a set of mean relaxation times (2, 40, and 121 ms). A triexponential fit with fixed relaxation times **(4)** was then performed using these relaxation times to identify changes in the amplitude of the slow component that may be attributed to muscle edema. These fits showed that the 11.83 MHz signals for all time points solely comprise the slow component corresponding to the subcutaneous tissue **(Figure 16d)**. This precludes the use of these measurements to identify muscle edema. In contrast, the amplitude of the same component in the 11.43 MHz signal responds to intramuscular interstitial fluid shifts concomitant with muscle edema. This signal shows a significant response to the onset of edema ($n = 42$ and 41, $p < 0.0001$, statistics by t test), its consistent progression ($n = 5$, $p < 0.0083$, statistics by significance of Spearman rank correlation), and its ultimate recovery towards baseline ($n = 52$ and 45, $p < 0.0001$, statistics by t test). This process was then repeated with a five exponential model (tau: 2, 40, 58, 121, and 226 ms) to capture the triexponential signal corresponding to the muscle and the biexponential signal corresponding to the subcutaneous fat tissue **(Figure 16e)**. The subcutaneous fat signal comprises the majority of the 11.83 MHz signal with a negligible fraction being assigned towards the muscle extracellular fluid (ECF). The muscle ECF signal in the 11.43 MHz signal responds to intramuscular fluid shifts while the amplitude of the subcutaneous fat signal remains approximately constant. This signal, once again, shows a significant response to the onset of edema ($n = 42$ and 41, $p < 0.0001$, statistics by t test), its consistent progression ($n = 5$, $p < 0.0083$, statistics by significance of Spearman rank correlation), and its ultimate recovery towards baseline ($n = 52$ and 45, $p < 0.0001$, statistics by t test). A small increase in the subcutaneous fat signal at 29 and 45 hours was likely leakage of the muscle ECF signal due to both increased amplitude and relaxation time as a result of the onset of edema.

The measurement of a region with a considerable fraction of subcutaneous tissue may be unavoidable, even with tuning of the RF excitation frequency, in cases of substantial subcutaneous thickness. In addition, it may be desirable to select a higher RF excitation frequency to decrease total acquisition time though the measurement may include some subcutaneous signal. In these cases, the aforementioned technique may be unable to resolve changes in the relaxation properties of the muscle. The use of a diffusion-weighted signal can help resolve signals originating from tissues or fluid compartments with distinct diffusivities. Measurements during the onset and recovery of muscle edema were performed at an RF excitation frequency of 11.60 MHz, representing a target region spanning both the subcutaneous tissue and the muscle tissue. These measurements were performed at an echo time of 65 μs, similarly to previous measurements, and an

additional echo time of 260 µs which applied increased diffusion weighting. The amplitudes of the slow component in a triexponential fit, corresponding primarily to the muscle ECF signal, at an echo time of 65 µs did not vary appreciably in response to muscle edema **(Figure 16f)**. This signal fails to identify the onset of edema ($n = 40$ and 39, $p = 1.0000$, statistics by t test) or its progression ($n = 5$, $p = 0.1167$, statistics by significance of Spearman rank correlation) though it does identify the recovery towards baseline ($n = 47$ and 39, $p < 0.0001$, statistics by t test). The amplitudes of this muscle ECF signal at an echo time of 260 µs decreased in response to muscle edema due to the increased diffusivity of water within the interstitial space *(52)*. This diffusion-weighted signal can enhance the signal corresponding to the muscle ECF without bias from the subcutaneous tissue signal **(Figure 16f)**. We first identify the expected muscle ECF signal fraction at an echo time of 260 µs based on the known sensitivity profile of the MR sensor at 11.60 MHz. The deviation from this baseline muscle ECF signal fraction observed in the 260 µs signal is due to the increased diffusivity of the muscle ECF in response to muscle edema, which we observe as signal attenuation. The difference of the 260 µs muscle ECF signal amplitude from the reference value is used to enhance the 65 µs muscle ECF amplitude. This adjusted signal more strongly accurately reflects identifies the expected expansion ($n = 5$, $p = 0.0417$, statistics by significance of Spearman rank correlation) and subsequent depletion ($n = 49$ and 41, $p < 0.0001$, statistics by t test) of the muscle ECF in response to muscle edema.

The portable MR sensor can identify the progression of acute muscle edema, which is utilized here as a model for fluid accumulation in the intramuscular ECF. In cases of moderate subcutaneous tissue thickness, the increased penetration depth offered by varying the RF excitation frequency serves to localize the measurement completely within the muscle tissue. In circumstances where the subcutaneous thickness is more substantial and localization by tuning the RF excitation frequency is insufficient, a diffusion-weighted measurement can help identify changes in the signal that are associated with fluid shifts within the intramuscular ECF. The combination of diffusion-weighted, depth-resolved multicomponent T2 relaxometry with a single-sided MR sensor offers the unique ability to identify shifts in tissue fluid distribution despite the presence of confounding tissue layers.

Chapter 4: Conclusion

3.3. *Clinical Impact*

The ability to accurately monitor the volume status of end-stage renal disease patients during hemodialysis would inform fluid removal and improve treatment outcomes *(6,15,32,34)*. Excess fluid removal induces intradialytic hypotension, which is associated with adverse outcomes including increased mortality and decreased long-term compliance with hemodialysis prescription *(4,6,37)*. The majority of patients undergoing hemodialysis will experience intradialytic hypotension *(36)*. Improved identification of overload in these patients may better inform fluid removal during hemodialysis to achieve dry weight while avoiding intradialytic hypotension *(14)*. A portable, non-invasive MR sensor of tissue fluid distribution can provide information on systemic volume status via measurements localized to the muscle *(44,47)*. Our prior clinical study demonstrated the need for improved measurement localization within the muscle to make an absolute determination of volume status.

3.4. *Future Work*

Several improvements to the MR sensor and the described methods could improve its ability to perform measurements of tissue fluid distribution. Diffusivity was not directly quantified in these measurements because of the presence of a spatially varying static magnetic field gradient and restricted diffusion within tissues *(25,53–56)*. Additional characterization of the sensor would be necessary to extract an accurate estimate of diffusivity. The CPMG pulse sequence was utilized to take advantage of its high sensitivity, robustness to field inhomogeneity and simplicity. Hardware limitations prevented implementation of more sophisticated pulse sequences that more directly enable estimation of sample diffusivity versus T2 *(57)*. An improved pulse sequence could simultaneously acquire depth-resolved, diffusion-weighted T2 measurements. In this work, we used an acute model of muscle edema in rodents. This served to provide an appropriate model to demonstrate the utility of these measurements. Future studies could investigate the physiology of systemic fluid overload in rodents or humans. Additionally, we simulated variability in subcutaneous tissue thickness with synthetic tissue phantoms. A subsequent study could assess this technology in human subjects with naturally varying subcutaneous thickness. We did not quantify water diffusivity or T2 within samples as this would require precise characterization of the static and RF magnetic fields of the sensor. Furthermore, restricted diffusion as observed in tissues creates a

complex multiexponential decay that further complicates quantitative analysis *(54–56,58)*. Quantitative parameter extraction is not necessary for this technology to provide diagnostic value as empirical thresholds can be derived through further clinical studies.

Works Cited

1. D.G. Nishimura, Principles of magnetic resonance imaging, Standford Univ., 2010.
2. F. Casanova, J. Perlo, B. Blumich, Single-Sided NMR, Springer, 2011.
3. M. Li, C.C. Vassiliou, L.A. Colucci, M.J. Cima, ^{1}H nuclear magnetic resonance (NMR) as a tool to measure dehydration in mice, NMR Biomed. **28** (2015) 1031–1039. doi:10.1002/nbm.3334.
4. J.E. Flythe, J.K. Inrig, T. Shafi, T.I. Chang, K. Cape, K. Dinesh, S. Kunaparaju, S.M. Brunelli, Association of intradialytic blood pressure variability with increased all-cause and cardiovascular mortality in patients treated with long-term hemodialysis, Am. J. Kidney Dis. **61** (2013) 966–974.
5. T.I. Chang, J. Paik, T. Greene, M. Desai, F. Bech, A.K. Cheung, G.M. Chertow, Intradialytic Hypotension and Vascular Access Thrombosis, J. Am. Soc. Nephrol. (2011) 1526–1533. doi:10.1681/ASN.2010101119.
6. R.F. Reilly, Attending rounds: A patient with intradialytic hypotension, Clin. J. Am. Soc. Nephrol. **9** (2014) 798–803. doi:10.2215/CJN.09930913.
7. M.Y. Zuidema, K.C. Dellsperger, Myocardial stunning with hemodialysis: clinical challenges of the cardiorenal patient, Cardiorenal Med. **2** (2012) 125–133.
8. A.M. Murray, Cognitive impairment in the aging dialysis and chronic kidney disease populations: an occult burden, Adv. Chronic Kidney Dis. **15** (2008) 123–132.
9. J.Q. Jaeger, R.L. Mehta, Assessment of dry weight in hemodialysis an overview, J. Am. Soc. Nephrol. **10** (1999) 392–403.
10. J.E. Flythe, S.E. Kimmel, S.M. Brunelli, Rapid fluid removal during dialysis is associated with cardiovascular morbidity and mortality, Kidney Int. **79** (2011) 250–257.
11. S.H.S. Huang, G. Filler, R. Lindsay, C.W. Mcintyre, Euvolemia in Hemodialysis Patients: A Potentially Dangerous Goal?, Semin. Dial. **28** (2015) 1–5. doi:10.1111/sdi.12317.
12. R. Agarwal, M.J. Andersen, J.H. Pratt, On the importance of pedal edema in hemodialysis patients, Clin. J. Am. Soc. Nephrol. **3** (2008) 153–158.
13. S. Ishibe, A.J. Peixoto, Methods of Assessment of Volume Status and Intercompartmental Fluid Shifts in Hemodialysis Patients: Implications in Clinical Practice, in: Semin. Dial., Wiley Online Library, 2004: pp. 37–43. doi:10.1111/j.1525-139X.2004.17112.x.

14. R. Agarwal, Volume Overload in Dialysis: The Elephant in the Room, No One Can See, Am. J. Nephrol. **38** (2013) 75–77. doi:10.1159/000353107.

15. S. McGee, W.B. Abernethy III, D.L. Simel, Is this patient hypovolemic?, Jama. **281** (1999) 1022–1029.

16. A. Bashyam, M. Li, M.J. Cima, Unilateral Linear Halbach magnets for single sided NMR: Generalized design framework and experimental validation, in: Proc. Int. Soc. Magn. Reson. Med. 2017 Annu. Meet., Honolulu, USA, 2017.

17. A. Bashyam, M. Li, M.J. Cima, Design and experimental validation of Unilateral Linear Halbach magnet arrays for single-sided magnetic resonance, J. Magn. Reson. (2018).

18. L.A. Colucci, Quantifying fluid overload with portable magnetic resonance sensors, Massachusetts Institute of Technology, 2018.

19. G. Eidmann, R. Savelsberg, P. Blümler, B. Blümich, The NMR MOUSE, a mobile universal surface explorer, J. Magn. Reson. Ser. A. **122** (1996) 104–109.

20. R. Möller, E. Tafeit, T.R. Pieber, K. Sudi, G. Reibnegger, Measurement of subcutaneous adipose tissue topography (SAT-Top) by means of a new optical device, LIPOMETER, and the evaluation of standard factor coefficients in healthy subjects, Am. J. Hum. Biol. Off. J. Hum. Biol. Assoc. **12** (2000) 231–239.

21. A.A. Istratov, O.F. Vyvenko, Exponential analysis in physical phenomena, Rev. Sci. Instrum. **70** (1999) 1233–1257.

22. F.R.E. Fenrich, C. Beaulieu, P.S. Allen, Relaxation times and microstructures, NMR Biomed. An Int. J. Devoted to Dev. Appl. Magn. Reson. Vivo. **14** (2001) 133–139.

23. G. Saab, R.T. Thompson, G.D. Marsh, Multicomponent T2 relaxation of in vivo skeletal muscle, Magn. Reson. Med. An Off. J. Int. Soc. Magn. Reson. Med. **42** (1999) 150–157.

24. S.J. Graham, P.L. Stanchev, M.J. Bronskill, Criteria for analysis of multicomponent tissue T2 relaxation data, Magn. Reson. Med. **35** (1996) 370–378.

25. P. Bendel, Spin-echo attenuation by diffusion in nonuniform field gradients, J. Magn. Reson. **86** (1990) 509–515.

26. D. Le Bihan, C. Poupon, A. Amadon, F. Lethimonnier, Artifacts and pitfalls in diffusion MRI, J. Magn. Reson. Imaging An Off. J. Int. Soc. Magn. Reson. Med. **24** (2006) 478–488.

27. S. Richard, B. Querleux, J. Bittoun, O. Jolivet, I. Idy-Peretti, O. de

Lacharriere, J.-L. Leveque, Characterization of the skin in vivo by high resolution magnetic resonance imaging: water behavior and age-related effects, J. Invest. Dermatol. **100** (1993) 705–709.

28. A.M. Heemskerk, B.M. Damon, Diffusion tensor MRI assessment of skeletal muscle architecture, Curr. Med. Imaging Rev. **3** (2007) 152–160.

29. G. Cotter, M. Metra, O. Milo-Cotter, H.C. Dittrich, M. Gheorghiade, Fluid overload in acute heart failure—re-distribution and other mechanisms beyond fluid accumulation, Eur. J. Heart Fail. **10** (2008) 165–169.

30. N. Albert, Fluid Management Strategies in Heart Failure, Crit. Care Nurse. **32** (2012) 20–32. doi:10.1016/B978-1-4377-1604-7.00058-0.

31. K. Kalantar-Zadeh, D.L. Regidor, C.P. Kovesdy, D. Van Wyck, S. Bunnapradist, T.B. Horwich, G.C. Fonarow, Fluid retention is associated with cardiovascular mortality in patients undergoing long-term hemodialysis, Circulation. **119** (2009) 671–679. doi:10.1161/CIRCULATIONAHA.108.807362.

32. D.E. Weiner, S.M. Brunelli, A. Hunt, B. Schiller, R. Glassock, F.W. Maddux, D. Johnson, T. Parker, A. Nissenson, Improving clinical outcomes among hemodialysis patients: A proposal for a "volume First" approach from the chief medical officers of us dialysis providers, Am. J. Kidney Dis. **64** (2014) 685–695. doi:10.1053/j.ajkd.2014.07.003.

33. S. Ishibe, A.J. Peixoto, Methods of assessment of volume status and intercompartmental fluid shifts in hemodialysis patients: Implications in clinical practice, Semin. Dial. **17** (2004) 37–43. doi:10.1111/j.1525-139X.2004.17112.x.

34. M.J.E. Dekker, J.P. Kooman, Fluid status assessment in hemodialysis patients and the association with outcome: Review of recent literature, Curr. Opin. Nephrol. Hypertens. **27** (2018) 188–193. doi:10.1097/MNH.0000000000000409.

35. J.J. Heidelbaugh, M. Sherbondy, Cirrhosis and Chronic Liver Failure: Part II. Complications and Treatment, Am. Fam. Physician. **74** (2006) 767–776. http://www.aafp.org/afp/2006/0901/p767.html.

36. J.J. Sands, L.A. Usvyat, T. Sullivan, J.H. Segal, P. Zabetakis, P. Kotanko, F.W. Maddux, J.A. Diaz-Buxo, Intradialytic hypotension: frequency, sources of variation and correlation with clinical outcome, Hemodial. Int. **18** (2014) 415–422.

37. T. Shoji, Y. Tsubakihara, M. Fujii, E. Imai, Hemodialysis-associated hypotension as an independent risk factor for two-year mortality in hemodialysis patients, Kidney Int. **66** (2004) 1212–1220. doi:10.1111/j.1523-1755.2004.00812.x.

38. Y. Dou, F. Zhu, P. Kotanko, Assessment of extracellular fluid volume and fluid status in hemodialysis patients: current status and technical advances, in: Semin. Dial., Wiley Online Library, 2012: pp. 377–387.

39. H.-M. Chung, R. Kluge, R.W. Schrier, R.J. Anderson, Clinical assessment of extracellular fluid volume in hyponatremia, Am. J. Med. **83** (1987) 905–908.

40. P.M. Kouw, J.P. Kooman, E.C. Cheriex, C.G. Olthof, P.M. de Vries, K.M. Leunissen, Assessment of postdialysis dry weight: a comparison of techniques., J. Am. Soc. Nephrol. **4** (1993) 98–104.

41. H. Nose, G.W. Mack, X.R. Shi, E.R. Nadel, Shift in body fluid compartments after dehydration in humans, J. Appl. Physiol. (Bethesda, Md. 1985). **65** (1988) 318–324. http://www.ncbi.nlm.nih.gov/pubmed/3403475.

42. H. Nose, T. Morimoto, K. Ogura, Distribution of water losses among fluid compartments of tissues under thermal dehydration in the rat., Jpn. J. Physiol. **33** (1983) 1019–29. doi:10.2170/jjphysiol.33.1019.

43. M. Horowitz, S. Samueloff, Plasma water shifts during thermal dehydration., J. Appl. Physiol. **47** (1979) 738–744.

44. L.A. Colucci, K.M. Corapi, M. Li, X.V. Parada, H.Y. Lin, D.A. Ausiello, M.S. Rosen, M.J. Cima, Bedside magnetic relaxometry for fluid assessment in end-stage renal disease, Under Rev. (2019).

45. Z. Ababneh, H. Beloeil, C.B. Berde, G. Gambarota, S.E. Maier, R. V. Mulkern, Biexponential parameterization of diffusion and T2 relaxation decay curves in a rat muscle edema model: decay curve components and water compartments, Magn. Reson. Med. An Off. J. Int. Soc. Magn. Reson. Med. **54** (2005) 524–531. doi:10.1002/mrm.20610.

46. C.J. Gordon, P.M. Phillips, A.F.M. Johnstone, A noninvasive method to study regulation of extracellular fluid volume in rats using nuclear magnetic resonance, Am. J. Physiol. - Ren. Physiol. **310** (2016) F426–F431. doi:10.1152/ajprenal.00405.2015.

47. A. Bashyam, C. Frangieh, M. Li, M.J. Cima, Dehydration assessment via a non-invasive, miniature, portable magnetic resonance sensor using multicomponent T2 relaxometry, Under Rev. (2019).

48. V. Demas, P.J. Prado, Compact Magnets for Magnetic Resonance, Concepts Magn. Reson. Part A Bridg. Educ. Res. (2009). doi:10.1002/cmr.a.20131.

49. A.E. Marble, I. V. Mastikhin, B.G. Colpitts, B.J. Balcom, A compact permanent magnet array with a remote homogeneous field, J. Magn. Reson. **186** (2007) 100–104. doi:10.1016/j.jmr.2007.01.020.

50. R. Bai, C.G. Koay, E. Hutchinson, P.J. Basser, A framework for accurate determination of the T2 distribution from multiple echo magnitude MRI

images, J. Magn. Reson. **244** (2014) 53–63. doi:10.1016/j.jmr.2014.04.016.

51. C.G. Koay, E. Özarslan, P.J. Basser, A signal transformational framework for breaking the noise floor and its applications in MRI, J. Magn. Reson. **197** (2009) 108–119.

52. R.H. Fan, M.D. Does, Compartmental relaxation and diffusion tensor imaging measurements in vivo in λ-carrageenan-induced edema in rat skeletal muscle, NMR Biomed. An Int. J. Devoted to Dev. Appl. Magn. Reson. Vivo. **21** (2008) 566–573.

53. P.N. Sen, A. André, S. Axelrod, Spin echoes of nuclear magnetization diffusing in a constant magnetic field gradient and in a restricted geometry, J. Chem. Phys. **111** (1999) 6548–6555.

54. S. Axelrod, P.N. Sen, Nuclear magnetic resonance spin echoes for restricted diffusion in an inhomogeneous field: Methods and asymptotic regimes, J. Chem. Phys. **114** (2001) 6878–6895.

55. T.M. de Swiet, P.N. Sen, Decay of nuclear magnetization by bounded diffusion in a constant field gradient, J. Chem. Phys. **100** (1994) 5597–5604.

56. M.N. d'Eurydice, P. Galvosas, Measuring diffusion–relaxation correlation maps using non-uniform field gradients of single-sided NMR devices, J. Magn. Reson. **248** (2014) 137–145.

57. D.G. Rata, F. Casanova, J. Perlo, D.E. Demco, B. Blümich, Self-diffusion measurements by a mobile single-sided NMR sensor with improved magnetic field gradient, J. Magn. Reson. **180** (2006) 229–235.

58. D.S. Grebenkov, Multiexponential attenuation of the CPMG spin echoes due to a geometrical confinement, J. Magn. Reson. **180** (2006) 118–126. doi:10.1016/j.jmr.2006.01.014.